J. Fluid Mech. (1992), *vol.* 235, *pp.* 255–283
Printed in Great Britain

On forced internal waves in a rectangular trench

By FRANCIS C. K. TING

Ocean Engineering Program, Department of Civil Engineering, Texas A&M University, College Station, TX 77843, USA

(Received 26 April 1990 and in revised form 25 July 1991)

The generation of internal waves in a submarine rectangular trench by normally incident surface waves has been investigated through laboratory experiments and theory. A linear model was developed for small-amplitude, simple harmonic wave motions. In this model, the fluid outside the trench is homogeneous, and the fluid in the trench is composed of two homogeneous layers of different densities separated by a transition region of linear density variation; viscous dissipation is treated based on the assumption of a laminar boundary layer. In the experiments, the stratification in the trench was created using fresh water and salt water, and a scanning laser beam and detector system was used to measure the amplitude of internal waves. The study shows that, when the frequency of the surface waves corresponds to the natural frequency of internal waves, the amplitude of internal waves becomes large compared to the amplitude of surface waves. The natural frequency of oscillation of internal waves decreases as the thickness of the density interface increases and the depth of the lower fluid decreases. Two distinct classes of internal waves were observed, namely, standing internal waves when the lower fluid was deep, and travelling internal waves when the lower fluid was shallow. The linear model predicted the response curve for internal waves quite well in all the cases investigated. It was also found that the internal waves were strongly damped when the depth of the lower fluid was small compared to the wavelength of internal waves.

1. Introduction

This paper is concerned with the generation of internal waves in a submarine trench that is partially filled with a heavier fluid; the fluid outside the trench is homogeneous. The motivation for this work is the effects of waves on dredged navigation channels with a layer of fine sediment in suspension near the bottom. Such dense layers may result from the entrainment of fine bottom material by waves, currents, and the passage of ships. An example of a harbour where this type of dense lower layer is present is Europort (Holland), where the bottom was defined as a region where the specific gravity of the fluid was larger than 1.2 (Marine Board (National Research Council) 1983). The density-stratified fluid in these channels can have an influence on the kinematics around the perimeter of the trench as a result of internal waves generated in the trench. This is because large-amplitude internal waves within the trench could result in fluid velocities near the trench boundaries that may be significantly larger than those corresponding to a homogeneous fluid, leading to more serious bottom erosion. The dynamics of internal waves in a rectangular trench due to surface waves that propagate in a direction perpendicular to the longitudinal axis of the trench are discussed herein using the results of theory and controlled laboratory experiments.

The propagation of time-periodic water waves past a rectangular trench with a

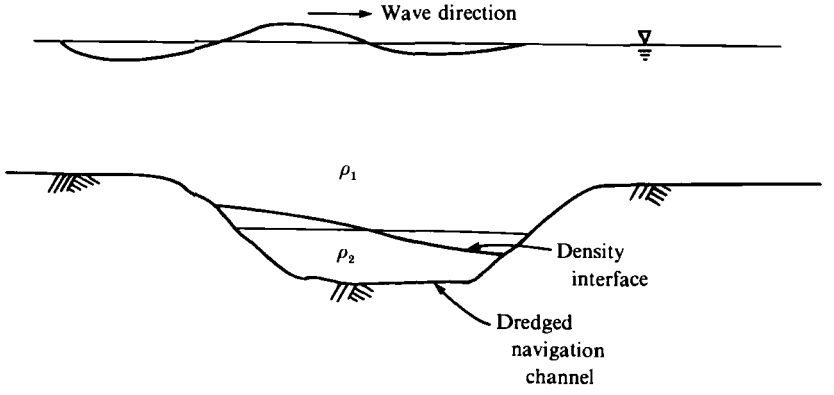

FIGURE 1. Schematic drawing of a dredged navigation channel.

homogeneous fluid in the trench has been studied by Lee & Ayer (1981), Miles (1982), and Kirby & Dalrymple (1983). Primary interests in those studies are related to the phenomenon of wave scattering, in which strong reflection of the incident waves can occur for suitable dimensions of the trench relative to the wavelength of the incident waves. It was found that for a particular symmetric trench where the water depths before and after the trench were equal, there existed an infinite number of discrete wave frequencies at which the incident wave energies were fully transmitted, the maximum and minimum values of the transmission and reflection coefficients appeared periodically, but the effect of the trench on wave energy transmission decreased monotonically as the wavelength decreased. Based on the formulation by Lee & Ayer (1982), Ting & Raichlen (1986) showed that the wave energies trapped within the trench were very small compared to the energies in the incident waves.

An important aspect of the interaction of surface waves with a density-stratified fluid in a submarine trench is the resonant oscillations of internal waves in the trench; this is illustrated in figure 1. The dynamic pressure associated with the surface waves induces a flow in the trench that displaces the heavier fluid and, through the action of buoyancy forces, generates internal waves that propagate to-and-fro between the walls of the trench. When the frequency of the surface waves corresponds to the natural frequency of the internal waves, the internal waves can attain large amplitudes relative to the surface waves. Thus, for a particular trench geometry relative to the characteristic lengthscale of the surface waves, the density-stratified fluid within the trench may be excited into a mode of resonant oscillation.

The excitation of internal waves in a rectangular trench by normally incident surface waves has been studied experimentally and theoretically by Ting & Raichlen (1988). Their analysis dealt with small-amplitude waves and an inviscid two-layer fluid in the trench, whereas fresh water and salt water were used to create the density stratification in the experiments. It was observed that at resonance the amplitude of the internal waves was large compared to the amplitude of the surface waves, but the effects of the internal waves on the surface waves were not measurable. The theoretical solutions predicted the wave motions quite well even for relatively large-amplitude waves in the trench.

In this study the effects of a diffuse density interface are examined; a continuously stratified fluid in the trench is approximated by a three-layer fluid that is composed of two homogeneous fluids of different densities separated by a transition region of linear density variation. In order to formulate this problem analytically, the Boussinesq approximation is made. This neglects variations of density in the

Navier–Stokes equations in so far as they affect inertia, but retains them in the buoyancy term. Thus, the three-layer model is limited in its application to a fluid whose overall density variations are small. It will also be assumed that the fluid motions in the trench are excited by small-amplitude water waves. Viscous dissipation will be treated based on the assumption of a laminar boundary layer. It is noted that laminar flow is applicable mainly to laboratory conditions, and is used here merely to show the sensitivity of the internal wave motions to viscous effects. Wall friction plays an important role in internal wave damping in submarine trenches. This is because if the effects of flow separation at the edges of the trench are neglected, the amplitudes of the internal waves are limited only by boundary friction and radiation losses. Radiation losses represent the energies in the waves scattered by the trench, but in this case the stratified fluid is confined to the trench so that the energies of the internal waves are largely trapped within the trench.

The nature of the internal waves in the trench is a major interest in this study. Thorpe (1968) has made an extensive study, both theoretical and experimental, of standing internal waves at the interface of two fluids and in a continuously stratified fluid. For the two-layer problem, his method of analysis was similar to the perturbation scheme in Stokes waves. Thorpe (1968) represented the finite-amplitude wave solutions in the form of power series expansions with respect to the wave slope as the expansion parameter. As in Stokes waves, the second-order term of the internal wave solution distorted the symmetric waveform of the linear solution given by the first-order term, whereas the distance from trough to crest remained the same for the second-order approximation. The ratio of the coefficient of the second-order term to that of the first therefore represented a measure of nonlinear effects in the internal waves. Thorpe (1968) showed that the presence of the upper fluid reduced the amplitude of the higher harmonics in the wave profile. This conclusion was previously reached by Hunt (1961), who studied standing waves at the interface between two semi-infinite fluids. Using the results of theory and experiments, we shall demonstrate that, for weakly nonlinear internal waves, a linear model of wave–trench interaction can predict the wave motions in a laboratory trench quite well, even for relatively large-amplitude waves in the trench.

Thorpe's finite-amplitude wave theory becomes invalid when the depth of the stratified fluid is so small compared to the wavelength of the internal wave that the ratio of the amplitude of the second harmonic to that of the first is of order unity. In this case the theory of long waves should be used to formulate the problem. Benjamin (1966) demonstrated that, for internal waves whose wavelengths were very large compared to the total fluid depth, the relative importance of nonlinear effects to dispersive effects was indicated by the ratio $\epsilon H_0 l_0^2/h_0^3$, which for waves of permanent form was of order unity. Here, H_0, l_0, and h_0 refer to a characteristic wave height, wavelength and depth, and ϵ represents the fractional change in density over the depth of the fluid. Benjamin (1967) considered a different situation in which the density of the fluid varied only within a layer whose thickness was much smaller than the wavelength of the internal wave, while the total depth of the fluid was infinite. In this case, $H_0 l/h_0^2$ was of order unity for internal waves of permanent form. The types of internal waves considered by Benjamin (1966, 1967) may be found in submarine trenches, and linear theory will not be applicable here. Long waves in a rectangular trench will be discussed with respect to experimental results.

The response of a fresh water–salt water fluid in a rectangular trench in a wave tank to surface waves generated by a bulkhead wave generator was studied by varying the surface wave height, the wave period, and the density stratification in

the trench. The major objectives of the experiments were to determine if the linear model developed was adequate or if it was necessary to use more complicated models, and to examine the importance of different physical effects such as density stratification and viscous dissipation on the dynamics of the wave–trench interaction.

2. Theoretical analysis

A definition sketch of the theoretical model is presented in figure 2. The fluid domain consists of a constant-depth channel connected to a rectangular trench at one end and a vertical boundary that moves in simple-harmonic motion at the opposite end. In early experiments, a beach was placed at the end of the wave tank to reduce the reflection of waves transmitted past the trench from the end of the tank. It was found that, owing to the long waves used, the amplitudes of the reflected waves were greater than 30% of those of the incident waves. Because of the reflections from the beach and, thus, the uncertain boundary condition at the beach, the theoretical predictions that were obtained using a model consisting of an infinite ocean and a rectangular trench could not be compared to these experimental results. Therefore, the theoretical model treated was changed from one consisting of an infinite ocean to the one shown in figure 2. This problem can be formulated theoretically and the results compared directly to the experimental measurements to establish the possibility of using the same theoretical approach for the case with the infinite region.

As shown in figure 2, the density distribution in the trench is represented by a three-layer fluid, which is composed of two homogeneous fluids of different densities separated by a transition region of linear density variation, and the density transition region is confined to the trench. The fluid is assumed to be inviscid and incompressible, but the fluid motion is not irrotational, owing to vorticity generated in the continuously stratified transition layer. A partial differential equation (Love's equation) can be obtained from the equations of motion by a standard perturbation procedure. For simple-harmonic motion, the Love's equation is reduced to a second-order ordinary differential equation with variable coefficients, which together with the boundary conditions, specify an eigenvalue problem. By applying the Boussinesq approximation to a three-layer fluid, the ordinary differential equation is changed into one with constant coefficients, which can be solved analytically. The solution in the trench region is expanded in terms of an infinite series of mutually orthogonal eigenfunctions. A similar procedure yields the series expansion solutions in the constant-depth channel. The horizontal and vertical velocities are matched along a vertical boundary at the edge of the trench to obtain a set of linear integral equations, which are solved numerically for the unknown coefficients.

2.1. *The eigenvalue problem*

Let (x, z) be a Cartesian coordinate system with z extending positive upwards from the undisturbed free surface and the bottom located at $z = -h_s$. The density of the fluid $\bar{\rho}$ is continuous in the interval $-h_s < z < 0$. The horizontal and vertical components of the fluid velocity in the positive x-direction and the positive z-direction are denoted by $u(x, z, t)$ and by $w(x, z, t)$, respectively. We shall investigate steady-state wave motion of the form

$$w(x, z, t) = f(z)\, e^{i(Kx-\sigma t)}, \tag{1}$$

in which K is the wavenumber and σ is the circular frequency.

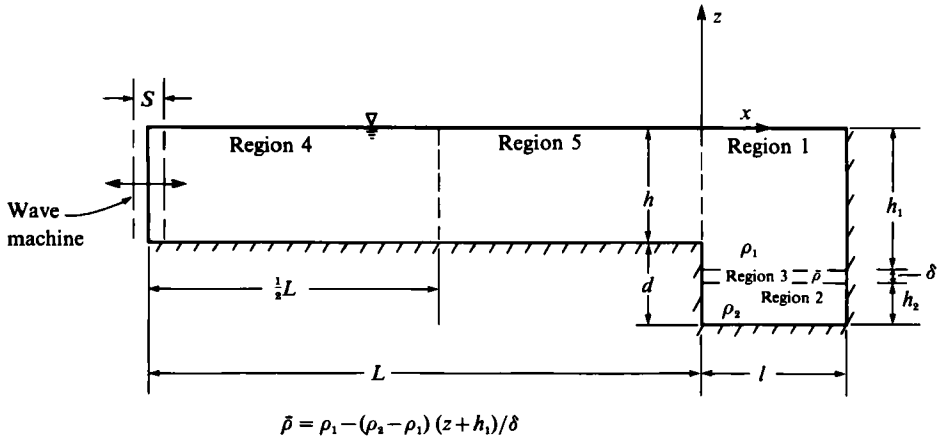

FIGURE 2. Definition sketch of the three-layer model.

Let the density variation in the quiescent fluid be small compared to a fluid density ρ_0, the Boussinesq approximation may then be made, and the linear governing equation for the vertical velocity is (see, for example, Yih 1980)

$$\frac{\mathrm{d}^2 f}{\mathrm{d}z^2} + K^2\left(\frac{\mathcal{N}^2}{\sigma^2} - 1\right) f = 0. \tag{2}$$

In (2), $\mathcal{N}$ is the buoyancy frequency (Brunt–Väisälä frequency) given by

$$\mathcal{N}^2(z) = -\frac{g}{\rho_0}\frac{\mathrm{d}\bar{\rho}}{\mathrm{d}z}. \tag{3}$$

The boundary condition on the free surface is

$$\frac{\mathrm{d}f}{\mathrm{d}z} - \frac{gK^2}{\sigma^2} f = 0 \quad \text{on} \quad z = 0, \tag{4}$$

and the boundary condition on the bottom is

$$f(z) = 0 \quad \text{on} \quad z = -h_s. \tag{5}$$

Note that f and $\mathrm{d}f/\mathrm{d}z$ are continuous in the interval $-h_s < z < 0$, and $\mathrm{d}^2 f/\mathrm{d}z^2$ is continuous in the region where $\mathrm{d}\bar{\rho}/\mathrm{d}z$ is continuous.

Equations (2)–(5) specify an eigenvalue problem. We are interested in the case where σ is held fixed and K^2 is the eigenvalue parameter. This is not a standard Sturm–Liouville problem because the eigenvalue parameter occurs in the free surface boundary condition. We put (2)–(5) in a vector form so that we can do the eigenfunction expansion. Consider the space of vectors with the first component a trial function and the second component a scalar; for any two such vectors U and V given by

$$U = \begin{pmatrix} \phi(z) \\ \phi_0 \end{pmatrix}, \quad V = \begin{pmatrix} \psi(z) \\ \psi_0 \end{pmatrix}, \tag{6}$$

we define the inner product

$$(U, V) = \int_{-h_s}^{0} \phi\psi \,\mathrm{d}z - \phi_0 \psi_0. \tag{7}$$

We further specify a subspace S of vectors such that $\phi(-h_s) = 0$ and $\phi_0 = \phi(0)$. Then all vectors $\boldsymbol{U} \in S$ are of the form

$$\boldsymbol{U}(z) = \begin{pmatrix} \phi(z) \\ \phi(0) \end{pmatrix} \quad \text{and} \quad \phi(-h_s) = 0. \tag{8}$$

Let

$$\mathscr{L}\boldsymbol{U} \equiv -\begin{pmatrix} \dfrac{\mathrm{d}^2\phi}{\mathrm{d}z^2}(z) \\ \dfrac{\mathrm{d}\phi}{\mathrm{d}z}(0) \end{pmatrix} \tag{9}$$

then our original eigenvalue problem can be stated as follows:

$$\mathscr{L}\boldsymbol{U} = \alpha \boldsymbol{R}\boldsymbol{U}, \quad \boldsymbol{U} \in S, \tag{10}$$

where

$$\alpha = K^2, \quad \boldsymbol{R} = \begin{pmatrix} \dfrac{\mathscr{N}^2}{\sigma^2} - 1 & 0 \\ 0 & -\dfrac{g}{\sigma^2} \end{pmatrix}. \tag{11}$$

The eigenvalue problem specified by (10) and (11) is self-adjoint, that is,

$$(\mathscr{L}\boldsymbol{U}, \boldsymbol{V}) = (\boldsymbol{U}, \mathscr{L}\boldsymbol{V}). \tag{12}$$

For any two different eigenvalues of the adjoint problem α and β, and their corresponding eigenvectors $\boldsymbol{U}$ and $\boldsymbol{V}$, it follows from (12) that

$$(\boldsymbol{R}\boldsymbol{U}, \boldsymbol{V}) = 0 \quad (\alpha \neq \beta). \tag{13}$$

It can be shown that each eigenvalue corresponds to only one eigenvector. Now that we have the orthogonality condition (13), we may expand a given vector $\boldsymbol{F}(z)$ in terms of a series of these eigenvectors, in the form

$$\boldsymbol{F}(z) = \begin{pmatrix} f(z) \\ f(0) \end{pmatrix} = \sum_{n=1}^{\infty} C_n \boldsymbol{U}_n(z), \tag{14}$$

where

$$C_n = \frac{(\boldsymbol{R}\boldsymbol{F}, \boldsymbol{U}_n)}{(\boldsymbol{R}\boldsymbol{U}_n, \boldsymbol{U}_n)}, \quad \boldsymbol{U}_n(z) = \begin{pmatrix} \phi_n(z) \\ \phi_n(0) \end{pmatrix}. \tag{15}$$

Equations (13) and (14) give the orthogonality condition and the eigenfunction expansion for the original problem. It can be shown that the eigenvalues are real, but the positive and negative values of K^2 have no upper and lower bounds. The positive values of K^2 correspond to the wavenumbers of the propagating waves while the negative values of K^2 correspond to the wavenumbers of the locally bounded standing waves that do not propagate. For arbitrary density distribution, (2)–(5) must be solved numerically for the eigenvalues and eigenfunctions. Analytical solutions for a homogeneous fluid and for a three-layer fluid are presented next.

2.1.1. *Eigenvalues and eigenfunctions of a homogeneous fluid*

The bottom of the constant-depth channel is specified at $z = -h$. The normalized eigenfunctions corresponding to (2)–(5) with $\mathscr{N} = 0$ are listed in the Appendix and are denoted by Z and $\hat{Z}_n$ $(n = 1, 2, \ldots)$. Any two such eigenfunctions $\phi(z)$ and $\psi(z)$ are orthogonal in the sense that

$$-\int_{-h}^{0} \phi\psi \, \mathrm{d}z + \frac{g}{\sigma^2}\phi(0)\psi(0) = \begin{cases} 0, & \phi \neq \psi; \\ 1, & \phi = \psi. \end{cases} \tag{16}$$

The corresponding eigenvalues k^2 and $-\hat{k}_n^2$ $(n = 1, 2, \ldots)$ are defined by the following relationships:

$$\sigma^2 = gk \tanh kh, \tag{17}$$

$$\sigma^2 = g\hat{k}_n \tan \hat{k}_n h \quad (n = 1, 2, \ldots). \tag{18}$$

2.1.2. *Eigenvalues and eigenfunctions of a three-layer fluid*

For the three-layer fluid in the trench, $\mathcal{N} = 0$ in $-(h_1+h_2+\delta) < z < -(h_1+\delta)$ and in $-h_1 < z < 0$, and $\mathcal{N} = \bar{\mathcal{N}} = (g\Delta\rho/\rho_1\delta)^{\frac{1}{2}}$ in $-(h_1+\delta) < z < -h_1$. The eigenvalues are defined by the following relationships:

$$\Theta^{\frac{1}{2}} \cos(\Theta^{\frac{1}{2}} K_j \delta)\left(\coth K_j h_2 + \frac{K_j \cosh K_j h_1 - K_0 \sinh K_j h_1}{K_j \sinh K_j h_1 - K_0 \cosh K_j h_1}\right)$$

$$-\sin(\Theta^{\frac{1}{2}} K_j \delta)\left(\Theta - \frac{K_j \cosh K_j h_1 - K_0 \sinh K_j h_1}{K_j \sinh K_j h_1 - K_0 \cosh K_j h_1} \coth K_j h_2\right) = 0 \quad (j = 1, 2, \ldots), \tag{19}$$

and

$$\Theta^{\frac{1}{2}} \cosh(\Theta^{\frac{1}{2}} \hat{K}_n \delta)\left(\cot \hat{K}_n h_2 + \frac{\hat{K}_n \cos \hat{K}_n h_1 - K_0 \sin \hat{K}_n h_1}{\hat{K}_n \sin \hat{K}_n h_1 + K_0 \cos \hat{K}_n h_1}\right)$$

$$+\sinh(\Theta^{\frac{1}{2}} \hat{K}_n \delta)\left(\Theta + \frac{\hat{K}_n \cos \hat{K}_n h_1 - K_0 \sin \hat{K}_n h_1}{\hat{K}_n \sin \hat{K}_n h_1 + K_0 \cos \hat{K}_n h_1} \cot \hat{K}_n h_2\right) = 0 \quad (n = 1, 2, \ldots), \tag{20}$$

in which $\Theta = (\bar{\mathcal{N}}^2/\sigma^2 - 1) \neq 0$, $K_0 = \sigma^2/g$, and K_j^2 $(j = 1, 2, \ldots)$ and $-\hat{K}_n^2$ $(n = 1, 2, \ldots)$ are the eigenvalues of K^2. Equation (19) has an infinite number of roots of K_j if and only if $\Theta > 0$. The smallest root K_1 is the wavenumber of the surface mode. The next root K_2 is the wavenumber of the primary internal mode. The surface mode and the primary internal mode usually have wavelengths much larger than δ, so that $K\delta \ll 1$ and (19) may be approximated by

$$\sigma^4(\coth K_j h_1 \coth K_j h_2 + 1 + K_j \delta(\coth K_j h_1 + \coth K_j h_2))$$

$$-\sigma^2\left(\frac{\rho_2}{\rho_1} \coth K_j h_1 + \coth K_j h_2 + K_j \delta(\coth K_j h_1 \coth K_j h_2 + 1)\right) g K_j$$

$$+\left(\frac{\rho_2}{\rho_1} - 1\right) g^2 K_j^2 = 0 \quad (j = 1, 2). \tag{21}$$

Equation (21) is similar to the dispersion relation for a two-layer fluid:

$$\sigma^4\left(\frac{\rho_2}{\rho_1} \coth K_j h_1 \coth K_j h_2 + 1\right) - \sigma^2 \frac{\rho_2}{\rho_1}(\coth K_j h_1 + \coth K_j h_2) g K_j$$

$$+\left(\frac{\rho_2}{\rho_1} - 1\right) g^2 K_j^2 = 0 \quad (j = 1, 2). \tag{22}$$

Note that (21) does not reduce to (22) exactly when $K_j\delta = 0$, which is due to the Boussinesq approximation; in the three-layer model the density ratio ρ_2/ρ_1 in the inertia term is approximated by unity. Equation (21) indicates that when $K_j\delta$ is small, the wavenumbers for the first two propagating modes of the three-layer fluid would be similar to the wavenumbers of the surface mode and the interfacial mode in a two-layer fluid. When $\Theta < 0$, the trigonometric functions sine and cosine in (19) become the hyperbolic sine and hyperbolic cosine, consequently K_j has only one real root corresponding to the wavenumber of the surface mode.

When $\Theta = 0$, the dispersion relation corresponding to (19) is given by the following for $\bar{\mathcal{N}} = \sigma$:

$$\sigma^2(\coth Kh_1 \coth Kh_2 + 1 + K\delta \coth Kh_2) = gK(\coth Kh_1 + \coth Kh_2 + K\delta \coth Kh_1 \coth Kh_2). \quad (23)$$

Equation (23) reduces to (17) when $K\delta = 0$. Equation (23) has only one real root corresponding to the wavenumber of the surface wave; there is no internal wave. Thus, internal waves in the three-layer fluid are possible only when $\sigma < \bar{\mathcal{N}}$; when $\sigma \geqslant \bar{\mathcal{N}}$ only the surface mode exists. In this study we are interested in the internal waves, hence the case $\Theta = 0$ will not be considered in the following analysis.

Equation (20) always has an infinite number of real roots; these are the wavenumbers of the locally bounded standing waves that do not propagate.

The normalized eigenfunctions of the three-layer fluid are denoted by $Z_{j1,2,3}$ and $\hat{Z}_{n1,2,3}$, $(j, n = 1, 2, \ldots)$ and are listed in the Appendix; the subscripts (1, 2, and 3) denote the respective regions shown in figure 2. Any two eigenfunctions ϕ and ψ are orthogonal in the sense that

$$\int_{-(h_1+h_2+\delta)}^{0} \left(\frac{\mathcal{N}^2}{\sigma^2} - 1\right) \phi\psi \, \mathrm{d}z + \frac{g}{\sigma^2}\phi(0)\,\psi(0) = \begin{cases} 0, & \phi \neq \psi; \\ 1, & \phi = \psi. \end{cases} \quad (24)$$

2.2. *The trench model*

The fluid domain is divided into five regions as shown in figure 2:

Region 1 $\bar{\rho} = \rho_1, \quad -h_1 < z < 0, \quad 0 < x < l;$

Region 2 $\bar{\rho} = \rho_2, \quad -(h_1+h_2+\delta) < z < -(h_1+\delta), \quad 0 < x < l;$

Region 3 $\bar{\rho} = \rho_1 - \Delta\rho(z+h_1)/\delta, \quad -(h_1+\delta) < z < -h_1, \quad 0 < x < l;$

Region 4 $\bar{\rho} = \rho_1, \quad -h < z < 0, \quad -L < x < \frac{1}{2}L;$

Region 5 $\bar{\rho} = \rho_1, \quad -h < z < 0, \quad -\frac{1}{2}L < x < 0.$

In order to facilitate the numerical treatment of this problem we have divided the constant-depth channel into two regions (4 and 5) at $x = \frac{1}{2}L$. We assume that at this location the wave motion consists of the left- and right-going progressive waves only; the amplitudes of the locally bounded non-propagating standing waves may be neglected when $h/L \ll 1$ because their amplitudes decay exponentially with distance from $x = 0$ and $x = -L$.

For steady-state motion, the horizontal velocity and the vertical velocity may be written in the form

$$u(x, z, t) = u'(x, z)\,\mathrm{e}^{-\mathrm{i}\sigma t}, \quad (25)$$

$$w(x, z, t) = w'(x, z)\,\mathrm{e}^{-\mathrm{i}\sigma t}. \quad (26)$$

The spatial velocities $u'(x, z)$ and $w'(x, z)$ may be expanded in terms of a series of the orthogonal modes found in §2.1. Keeping in mind that u' and w' must satisfy the continuity equation, the solutions in the trench region are written as

$$u'_{1,2,3}(x, z) = \sum_{j=1}^{\infty} \frac{i}{K_j}(A_j \mathrm{e}^{\mathrm{i}K_j x} - B_j \mathrm{e}^{-\mathrm{i}K_j x}) \frac{\mathrm{d}}{\mathrm{d}z}(Z_{j1,2,3}(z)) - \sum_{n=1}^{\infty} \frac{1}{\hat{K}_n}(\hat{A}_n \mathrm{e}^{\hat{K}_n x} - \hat{B}_n \mathrm{e}^{-\hat{K}_n x}) \frac{\mathrm{d}}{\mathrm{d}z}(\hat{Z}_{n1,2,3}(z)), \quad (27)$$

$$w'_{1,2,3}(x, z) = \sum_{j=1}^{\infty} (A_j \mathrm{e}^{\mathrm{i}K_j x} + B_j \mathrm{e}^{-\mathrm{i}K_j x}) Z_{j1,2,3}(z) + \sum_{n=1}^{\infty} (\hat{A}_n \mathrm{e}^{\hat{K}_n x} + \hat{B}_n \mathrm{e}^{-\hat{K}_n x}) \hat{Z}_{n1,2,3}(z), \quad (28)$$

where A_j, B_j $(j = 1, 2, \ldots)$, and $\hat{A}_n, \hat{B}_n$ $(n = 1, 2, \ldots)$ are unknown constants to be determined from the boundary and matching conditions. The solutions in the constant-depth channel are written as

$$u_4'(x,z) = \frac{\mathrm{i}}{k}(C\mathrm{e}^{\mathrm{i}k(x+L)} - D\mathrm{e}^{-\mathrm{i}k(x+L)})\frac{\mathrm{d}Z}{\mathrm{d}z}(z) + \sum_{n=1}^{\infty}\frac{1}{\hat{k}_n}\hat{C}_n\mathrm{e}^{-\hat{k}_n(x+L)}\frac{\mathrm{d}\hat{Z}_n}{\mathrm{d}z}(z), \tag{29}$$

$$u_5'(x,z) = \frac{\mathrm{i}}{k}(E\mathrm{e}^{\mathrm{i}kx} - F\mathrm{e}^{-\mathrm{i}kx})\frac{\mathrm{d}Z}{\mathrm{d}z}(z) - \sum_{n=1}^{\infty}\frac{1}{\hat{k}_n}\hat{F}_n\mathrm{e}^{\hat{k}_n x}\frac{\mathrm{d}\hat{Z}_n}{\mathrm{d}z}(z), \tag{30}$$

$$w_4'(x,z) = (C\mathrm{e}^{\mathrm{i}k(x+L)} + D\mathrm{e}^{-\mathrm{i}k(x+L)})Z(z) + \sum_{n=1}^{\infty}\hat{C}_n\mathrm{e}^{-\hat{k}_n(x+L)}\hat{Z}_n(z), \tag{31}$$

$$w_5'(x,z) = (E\mathrm{e}^{\mathrm{i}kx} + F\mathrm{e}^{-\mathrm{i}kx})Z(z) + \sum_{n=1}^{\infty}\hat{F}_n\mathrm{e}^{\hat{k}_n x}\hat{Z}_n(z), \tag{32}$$

in which C, D, E, F, and $\hat{C}_n, \hat{F}_n$ $(n = 1, 2, \ldots)$ are unknown constants to be determined.

The fluid velocities must satisfy the following additional boundary conditions:

$$u = 0 \quad \text{on} \quad -(h_1 + h_2 + \delta) < z < -h, \quad x = 0; \tag{33}$$

$$u = 0 \quad \text{on} \quad -(h_1 + h_2 + \delta) < z < 0, \quad x = l; \tag{34}$$

$$u_4 = \tfrac{1}{2}\mathrm{i}S\sigma\mathrm{e}^{-\mathrm{i}\sigma t} \quad \text{on} \quad -h < z < 0, \quad x = -L; \tag{35}$$

where S is the stroke of the wave generator. The matching conditions at $x = 0$ are

$$u_1 = u_5 \quad \text{on} \quad -h < z < 0, \quad x = 0; \tag{36}$$

$$w_1 = w_5 \quad \text{on} \quad -h < z < 0, \quad x = 0. \tag{37}$$

Equation (36) is the kinematic matching condition. The dynamic matching condition is the continuity of pressure. It can be shown that in the upper layer the pressure gradient is related to the vertical velocity by $\partial p/\partial z = \mathrm{i}\sigma\rho_1 w$, thus continuity of vertical velocity (equation (37)) implies that the pressure across $x = 0$ can differ only by a constant, which must be equal to zero from the dynamic free surface condition.

Equation (34) implies

$$B_j = A_j\mathrm{e}^{2\mathrm{i}K_j l} \quad (j = 1, 2, \ldots), \tag{38}$$

$$\hat{B}_n = \hat{A}_n\mathrm{e}^{2\hat{K}_n l} \quad (n = 1, 2, \ldots). \tag{39}$$

Integrating (35), we get

$$\frac{\mathrm{i}}{k}(C - D)Z(z) + \sum_{n=1}^{\infty}\frac{1}{\hat{k}_n}\hat{C}_n\hat{Z}_n(z) = \tfrac{1}{2}\mathrm{i}S\sigma(z + h). \tag{40}$$

The integration yields the volume flux between $-h$ and z, the constant of integration is determined from the condition that the volume flux must be zero at $z = -h$. Upon using (15), we obtain

$$C - D = \frac{S\sigma}{2k}(\Lambda^h)^{-\frac{1}{2}}\sinh kh, \tag{41}$$

$$\hat{C}_n = -\frac{\mathrm{i}S\sigma}{2\hat{k}_n}(\Lambda_n^h)^{-\frac{1}{2}}\sin\hat{k}_n h, \tag{42}$$

where the normalization constants Λ^h and Λ_n^h are listed in the Appendix.

We assume that the wave motion is asymptotically a superposition of simple wave trains at $x = -\frac{1}{2}L$, hence

$$E = C\mathrm{e}^{\mathrm{i}kL}, \tag{43}$$

$$F = D\mathrm{e}^{-\mathrm{i}kL}. \tag{44}$$

2.2.1. *Matching the solutions*

We truncate the infinite series in (27)–(32) after a finite number of terms, given by J for the propagating modes and N for the non-propagating modes. We are then left with $(J+2N+1)$ unknowns: A_j $(j = 1, 2, \ldots, J)$, C, and $\hat{A}_n$, $\hat{F}_n$ $(n = 1, 2, \ldots, N)$. We obtain $(J+2N+1)$ equations by matching the horizontal and vertical velocities in the trench region and in the constant-depth channel along a vertical boundary at $x = 0$. First we consider the condition of continuity of horizontal velocity at $x = 0$. Integrating (27) between $-(h_1+h_2+\delta)$ and z, we obtain the volume flux $\tilde{Q}(z)$ at $x = 0$:

$$\tilde{Q}_{1,2,3}(z) = \sum_{j=1}^{J} \frac{\mathrm{i}}{K_j}(A_j - B_j) Z_{j1,2,3}(z) - \sum_{n=1}^{N} \frac{1}{\hat{K}_n}(\hat{A}_n - \hat{B}_n)\hat{Z}_{n1,2,3}(z), \tag{45}$$

in which $\tilde{Q}_i$ $(i = 1, 2, 3)$ denotes the volume flux between $-(h_1+h_2+\delta)$ and z in region i. Integrating (30) between $-h$ and z, we get

$$\tilde{Q}_5(z) = \frac{\mathrm{i}}{k}(E-F)Z(z) - \sum_{n=1}^{N} \frac{1}{\hat{k}_n}\hat{F}_n \hat{Z}_n(z). \tag{46}$$

Equations (33) and (36) imply that

$$\tilde{Q}_1(z) = \tilde{Q}_5(z), \quad -h < z < 0; \tag{47}$$

$$\tilde{Q}_1(z) = 0, \quad -h_1 < z < -h; \tag{48}$$

$$\tilde{Q}_2(z) = 0, \quad -(h_1+h_2+\delta) < z < -(h_1+\delta); \tag{49}$$

$$\tilde{Q}_3(z) = 0, \quad -(h_1+\delta) < z < -h_1. \tag{50}$$

Note that $\tilde{Q}_i$ is continuous in z, and the matching is done over the larger depth $(h_1+h_2+\delta)$ in order to satisfy the boundary condition on the upstream wall of the trench (equation (33)). Upon using (15), we obtain $(J+N)$ linear integral equations:

$$\frac{\mathrm{i}}{K_j}(A_j - B_j) = -\int_{-h}^{0} \tilde{Q}_5(z) Z_{j1}(z)\,\mathrm{d}z + \frac{g}{\sigma^2}\tilde{Q}_5(0) Z_{j1}(0) \quad (j = 1, 2, \ldots, J), \tag{51}$$

$$-\frac{1}{\hat{K}_n}(\hat{A}_n - \hat{B}_n) = -\int_{-h}^{0} \tilde{Q}_5(z)\hat{Z}_{n1}(z)\,\mathrm{d}z + \frac{g}{\sigma^2}\tilde{Q}_5(0)\hat{Z}_{n1}(0) \quad (n = 1, 2, \ldots, N). \tag{52}$$

The remaining $(N+1)$ equations are constructed from the condition of continuity of vertical velocity at $x = 0$. In this case, we only need to be concerned with the vertical velocities in the interval between $-h$ and 0. The results are

$$E + F = -\int_{-h}^{0} \tilde{w}_1'(0, z) Z(z)\,\mathrm{d}z + \frac{g}{\sigma^2}\tilde{w}_1'(0, 0) Z(0), \tag{53}$$

$$\hat{F}_n = -\int_{-h}^{0} \tilde{w}_1'(0, z)\hat{Z}_n(z)\,\mathrm{d}z + \frac{g}{\sigma^2}\tilde{w}_1'(0, 0)\hat{Z}_n(0) \quad (n = 1, 2, \ldots, N). \tag{54}$$

The integrals in (51)–(54) can be evaluated in terms of trigonometric functions and hyperbolic functions. The set of $(J+2N+1)$ simultaneous equations are solved numerically as a linear matrix equation. After the coefficients are found, the

horizontal and vertical velocities at $x = 0$ are computed and the matching conditions are checked for the solution accuracy. We found, numerically, that the series expansions for the three-layer fluid converge much faster than those for the homogeneous fluid, so that the contributions of the non-propagating modes to the series expansions are negligible after the first few terms. However, a series with a large number of terms does make the matrix equation more ill-conditioned, consequently the accuracy of the solution declines. In the numerical analysis, we have used $J = 2$ and $N = 3$, which give a good match of the horizontal velocity and the vertical velocity at $x = 0$. Since the density gradient at the interface was quite large in our experiments, the free surface mode and the primary internal mode dominate the wave motion in the trench region.

2.2.2. *Analysis of wave amplitude*

After the unknown coefficients are found, the velocities are determined for the entire fluid domain. Our main interest in this problem is the amplitude of the internal wave relative to the amplitude of the surface wave. From linear theory, the vertical displacement η of a fluid element from its undisturbed position is given by

$$\eta(x, z, t) = \int w \, \mathrm{d}t = \frac{\mathrm{i}}{\sigma} w' \mathrm{e}^{-\mathrm{i}\sigma t}. \tag{55}$$

We define the amplification factor R as the ratio of the internal wave amplitude at $x = 0$ to the surface wave amplitude at $x = l$, that is,

$$R(z) = \frac{|\eta(0, z, t)|}{|\eta(l, 0, t)|}. \tag{56}$$

The phase shift θ between the internal motion and the surface motion at these locations is given by

$$\theta(z) = \arg\{\eta(0, z, t)\} - \arg\{\eta(l, 0, t)\}, \tag{57}$$

where 'arg' is the argument of a complex number.

2.3. *Wave damping*

The arrangement chosen for theoretical analysis is a closed system so that the wave amplitudes predicted by an inviscid theory will tend to infinity at resonance. This singularity can be removed by including viscous effects in the theoretical model.

Since the viscosity of water is very small, viscous dissipation is significant only in the boundary layers adjacent to the sidewalls and the bottom of the wave tank. In addition, the boundary layers are very thin so that the overall fluid motion outside the boundary layers can be predicted well by the inviscid solutions. The effect of viscosity on the propagating waves is to cause a slow attenuation of the wave amplitude with distance and to decrease the phase speed and the wavelength. Viscosity has negligible effects on the non-propagating local disturbances because their amplitudes decay exponentially with distance from the trench and from the wave generator. Hence, viscous effects are treated by replacing the real-valued wavenumbers of the propagating waves in the exponents in (27)–(32) by complex-valued wavenumbers; the real part of the complex wavenumber is related to the wavelength, and the imaginary part gives the spatial attenuation rate. The velocities at $x = 0$ are matched as before; thus the equations in §2.2 are otherwise unchanged. This approach is valid because the boundary layers are very thin, so that the overall fluid motion may be treated as inviscid.

Mei & Liu (1973) have found the complex wavenumber for time-periodic progressive waves in a homogeneous fluid in a rectangular channel. Writing the complex wavenumber as $k+(1+\mathrm{i})k^*$, then k is that part of the wavenumber obtained using inviscid theory (equation (17)) and is real; the part $(1+\mathrm{i})k^*$ is due to the viscosity, with k^* given by

$$k^* = \frac{k}{b}\left(\frac{\nu}{2\sigma}\right)^{\frac{1}{2}}\left(\frac{2kb+\sinh 2kh}{2kh+\sinh 2kh}\right), \tag{58}$$

where $2b$ is channel width, and ν is the kinematic viscosity.

We now present the complex wavenumber for progressive waves in a three-layer fluid. Let (x, y, z) be a Cartesian coordinate system with the x-axis on the undisturbed free surface coinciding with the channel axis and z extending positive upwards. The sidewalls of the rectangular channel are located at $y = b$ and $y = -b$. The rate of amplitude attenuation is found by balancing the difference in the flux of wave energy between two vertical sections of the channel to the rate of energy loss in the fluid between the two vertical sections. For waves travelling in the positive x-direction, the horizontal velocity, the vertical velocity, and the dynamic pressure can be written as follows (see Yih 1980):

$$u(x,z,t) = \frac{\mathrm{i}}{K}\frac{\mathrm{d}f}{\mathrm{d}z}A\mathrm{e}^{\mathrm{i}(Kx-\sigma t)}, \tag{59}$$

$$w(x,z,t) = f(z)A\mathrm{e}^{\mathrm{i}(Kx-\sigma t)}, \tag{60}$$

$$p(x,z,t) = \mathrm{i}\rho_1\frac{\sigma}{K^2}\frac{\mathrm{d}f}{\mathrm{d}z}A\mathrm{e}^{\mathrm{i}(Kx-\sigma t)}, \tag{61}$$

where A is an arbitrary constant, and $f(z)$ is the eigenfunction of the three-layer fluid.

In the bottom boundary layer, the horizontal velocity u_{B} is given by the sum of the inviscid part u_0 and the viscous correction, that is,

$$u_{\mathrm{B}} = (1-\exp[-(\sigma/2\nu)^{\frac{1}{2}}(1-\mathrm{i})(z+h_1+h_2+\delta)])\,[u_0]_{z=-(h_1+h_2+\delta)}, \tag{62}$$

where the subscript B denotes the bottom. Denote the rectangular coordinates by x_i $(i = 1, 2, 3)$, with $x_1 = x, x_2 = y, x_3 = z$ and the corresponding velocity components by u_i. The average rate of energy dissipation over one wave period in a control volume is given by

$$\overline{\frac{\mathrm{d}E}{\mathrm{d}t}} = \frac{\rho\nu}{4}\int_V \left|\frac{\partial u_i}{\partial x_j}+\frac{\partial u_j}{\partial x_i}\right|^2 \mathrm{d}V, \tag{63}$$

where summation over repeated indices is implied. The principal contribution to (63) from the bottom boundary layer in the region between x and $x+\mathrm{d}x$ is given by

$$\left[\overline{\frac{\mathrm{d}E}{\mathrm{d}t}}\right]_{\mathrm{B}} = \left(\frac{\nu}{2\sigma}\right)^{\frac{1}{2}}\frac{\rho_1\sigma b\,\mathrm{d}x}{K^2}\left|\frac{\mathrm{d}f}{\mathrm{d}z}\right|^2_{z=-(h_1+h_2+\delta)}|A|^2. \tag{64}$$

By symmetry, we only need to consider the boundary layer adjacent to the sidewall $y = b$. The horizontal velocity and the vertical velocity are given by

$$u_{\mathrm{W}} = (1-\exp[-(\sigma/2\nu)^{\frac{1}{2}}(1-\mathrm{i})(b-y)])\,[u_0]_{y=b}, \tag{65}$$

$$w_{\mathrm{W}} = (1-\exp[-(\sigma/2\nu)^{\frac{1}{2}}(1-\mathrm{i})(b-y)])\,[w_0]_{y=b}, \tag{66}$$

where the subscript W denotes the sidewall. The net contribution to (63) from the sidewall boundary layers at $y = b$ and $y = -b$ is given by

$$\left[\frac{\overline{\mathrm{d}E}}{\mathrm{d}t}\right]_{\mathrm{W}} = \left(\frac{\nu}{2\sigma}\right)^{\frac{1}{2}} \frac{\rho_1 \sigma \,\mathrm{d}x}{K} \int_{-(h_1+h_2+\delta)}^{0} \left(\frac{1}{K}\left|\frac{\mathrm{d}f}{\mathrm{d}z}\right|^2 + K|f|^2\right) \mathrm{d}z |A|^2. \tag{67}$$

Equations (64) and (67) include all the energy losses that are proportional to $\nu^{\frac{1}{2}}$. It can be seen in (63) that energy dissipation in the density transition region is proportional to ν, and therefore is neglected at the present order of approximation. The average rate at which work is done over one wave period across a section of the rectangular channel is

$$\begin{aligned} \frac{\overline{\mathrm{d}W}}{\mathrm{d}t} &= \frac{2b}{T} \int_t^{t+T} \int_{-(h_1+h_2+\delta)}^{0} p_0 u_0 \,\mathrm{d}z \\ &= \frac{\rho_1 \sigma b}{K^2} \int_{-(h_1+h_2+\delta)}^{0} \frac{1}{K}\left|\frac{\mathrm{d}f}{\mathrm{d}z}\right|^2 \mathrm{d}z |A|^2. \end{aligned} \tag{68}$$

The difference between the energy crossing the planes x and $x+\mathrm{d}x$ is equal to the energy dissipated in the region between x and $x+\mathrm{d}x$. Define the attenuation rate K^* by

$$A = A_0 \mathrm{e}^{-K^* x}, \tag{69}$$

where A_0 is a constant. From (64), and (67)–(69) the attenuation rate K^* is found:

$$K^* = \frac{1}{2} \frac{\left(\frac{\nu}{2\sigma}\right)^{\frac{1}{2}} \left\{ \frac{b}{K}\left|\frac{\mathrm{d}f}{\mathrm{d}z}\right|^2_{z=-(h_1+h_2+\delta)} + \int_{-(h_1+h_2+\delta)}^{0} \left(\frac{1}{K}\left|\frac{\mathrm{d}f}{\mathrm{d}z}\right|^2 + K|f|^2\right) \mathrm{d}z \right\}}{\frac{b}{K} \int_{-(h_1+h_2+\delta)}^{0} \frac{1}{K}\left|\frac{\mathrm{d}f}{\mathrm{d}z}\right|^2 \mathrm{d}z}. \tag{70}$$

The integrals in (70) can be evaluated in terms of trigonometric and hyperbolic functions. Note that the method of energy balance does not yield the real part of the complex wavenumber, which is related to the wavelength. Dore (1969*a*, *b*) used a perturbation technique to obtain the complex wavenumber for non-homogeneous viscous fluids of general density and viscosity distributions. Dore showed that the viscous correction to the real part of the wavenumber is the same as the attenuation rate; thus the complex wavenumber is given by $K+(1+\mathrm{i})K^*$.

3. Experimental equipment and procedures

A schematic diagram of the experimental arrangement is shown in figure 3. The experiments were conducted in a wave tank 36.6 m long, 0.61 m deep, and 0.394 m wide with glass walls throughout. A horizontal plywood false bottom was placed in the wave tank to create a rectangular trench 0.6 m wide and 0.152 m deep. The upstream wall of the trench was located 19.15 m from a bulkhead wave generator. The portion of the wave tank downstream of the trench was not used in this study and was sealed off from the rest of the wave tank by a plywood vertical wall.

Time-periodic water waves were generated at one end of the tank by a bulkhead wave generator that moved in simple-harmonic motion. Wave period was measured using a digital counter that was accurate to 1/1000 s. The wave generator was controlled by an electrohydraulic servo-system. The system accepted an input voltage from a memory device that could store a 1000-point voltage time history; the

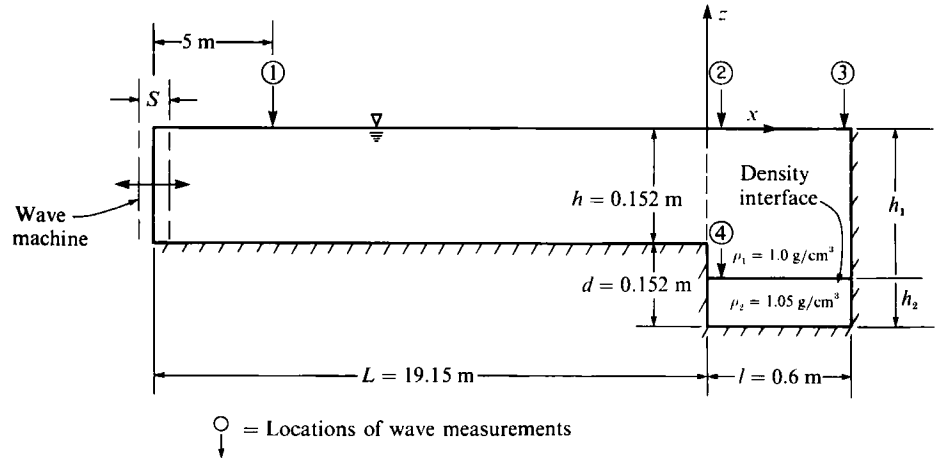

FIGURE 3. Experimental arrangement and locations of wave measurements.

displacement time history of the wave plate was proportional to the voltage time history of the input signal. A feedback system consisting of a linear variable differential transformer minimized the difference between the desired position of the wave plate and the actual position.

The experiments consisted of measurement of surface and internal wave amplitudes, and density stratifications. Surface wave amplitudes were measured using resistance wave gauges. Vertical positioning of the wave gauge during calibration was controlled by a stepping motor and was accurate to 1/30 mm. Internal wave amplitudes were measured using a scanning laser beam and detector system. A detailed description of this instrument can be found in Ting & Raichlen (1988). Density stratifications in the trench were created using fresh water and salt water, the latter being pre-mixed with blue dye to make the interface distinguishable. Density profiles were inferred from conductivity measurements that were made using a miniature four-electrode conductivity probe; a detailed discussion of the probe can be found in Head (1983). The probe was calibrated using 'standard' salt water solutions, and their exact densities were determined by weighing 100 cm³ of each solution in a volumetric flask.

Referring to figure 3, the depth of fresh water outside the trench was 15.2 cm; the trench was stratified with fresh water and salt water with a density difference of 5% relative to fresh water. The experiments were conducted for the following fluid depths in the trench: (i) $h_1 = 22.8$ cm, $h_2 = 7.6$ cm, (ii) $h_1 = 26.6$ cm, $h_2 = 3.8$ cm, and for two values of the interface thickness $\delta = 1.3$ cm and $\delta = 2.5$ cm. The depths h_1 and h_2 were respectively, measured from the undisturbed water surface and the trench bottom to the centre of the diffuse salinity interface. The interface thickness δ is defined as the ratio of the maximum density difference between fresh water and salt water to the maximum density gradient in the diffuse salinity interface, that is,

$$\delta = -\Delta\rho\left(\frac{\mathrm{d}\rho}{\mathrm{d}z}\right)^{-1}_{\max}, \tag{71}$$

where $\Delta\rho = \rho_2 - \rho_1$.

The response curves for internal waves were constructed from results of many experiments. The following procedure was used to ensure that the density stratifications were closely reproducible. The trench was stratified by first filling the wave tank with fresh water to a depth of 15.2 cm above the false bottom. Salt water

was then introduced through a port in the bottom of the trench. The filling process created a density interface of thickness between 2 and 2.5 cm, which was reduced to approximately 0.5 cm by selective withdrawal of fluid from the interface. The density profile was measured and the location of the dye interface was determined using the interfacial wave gauge (see Ting & Raichlen 1988). Then the stratified fluid was left undisturbed for 2–8 h. The experiments were conducted after the density interface had diffused to the required thickness. The interface thickness was determined from the density profile that was obtained 15 min after the experiment; the actual experiments took approximately 17 min. Hence this value corresponded to a steady-state condition in the trench.

The locations of the surface and internal wave measurements are shown in figure 3 and labelled as 1, 2, and 3 for the surface wave gauges and 4 for the interfacial wave gauge. The time histories of the wave plate motion and of the water surface and density interface were recorded simultaneously from the start of the wave generator until conditions in the wave tank had reached steady state.

4. Results and discussion

4.1. *Experiments with a deep lower fluid in the trench*

In these experiments, the depths h_1 and h_2 were 22.8 and 7.6 cm, respectively. The experiments were conducted for a range of wave periods associated with the lowest mode of oscillation of internal waves in the trench. Typical examples of density distribution in the trench are shown in figure 4(*a*, *b*). It is seen that the interface thickness increased during the experiment; this was due to wave-induced mixing and molecular diffusion. Wave-induced mixing was observed as gradual blurring of the dye interface, notably at the trench walls. This occasionally generated a spurious signal at the interfacial wave gauge, due to variation of the refractive index within the flow field. Nevertheless, the density interface remained stable in these experiments. For a surface of density discontinuity at $z = -h_1$ at some initial time $t = 0$, the density profile in the trench at a subsequent time t due to molecular diffusion is given by the following diffusion equation:

$$\rho = \rho_1 + \Delta\rho \operatorname{erfc}\left(\frac{z-h_1}{(4D_m t)^{\frac{1}{2}}}\right), \tag{72}$$

where D_m is the molecular diffusion coefficient, and erfc is the complementary error function. Substitution of (72) into (71) yields the following relationship for the interface thickness and the diffusion coefficient:

$$\delta = (4\pi D_m t)^{\frac{1}{2}}. \tag{73}$$

Hence, a diffusion coefficient can be calculated for the time interval $(t_2 - t_1)$ by

$$D_m = \frac{1}{4\pi}\left(\frac{\delta_{t_2}^2 - \delta_{t_1}^2}{t_2 - t_1}\right). \tag{74}$$

The molecular diffusion coefficient of salt in water was determined experimentally. The mean from thirteen tests was 1.31×10^{-5} cm^2 s^{-1}, and the standard deviation was 0.07×10^{-5} cm^2 s^{-1}. With wave motion, (74) gives an apparent diffusion coefficient, which represents the rate of mixing due to wave motions as well as molecular diffusion. For example, in figure 4(*a*) the interface thickness increased from 0.54 cm after selective withdrawal to 1.41 cm after the experiment, during a time interval of

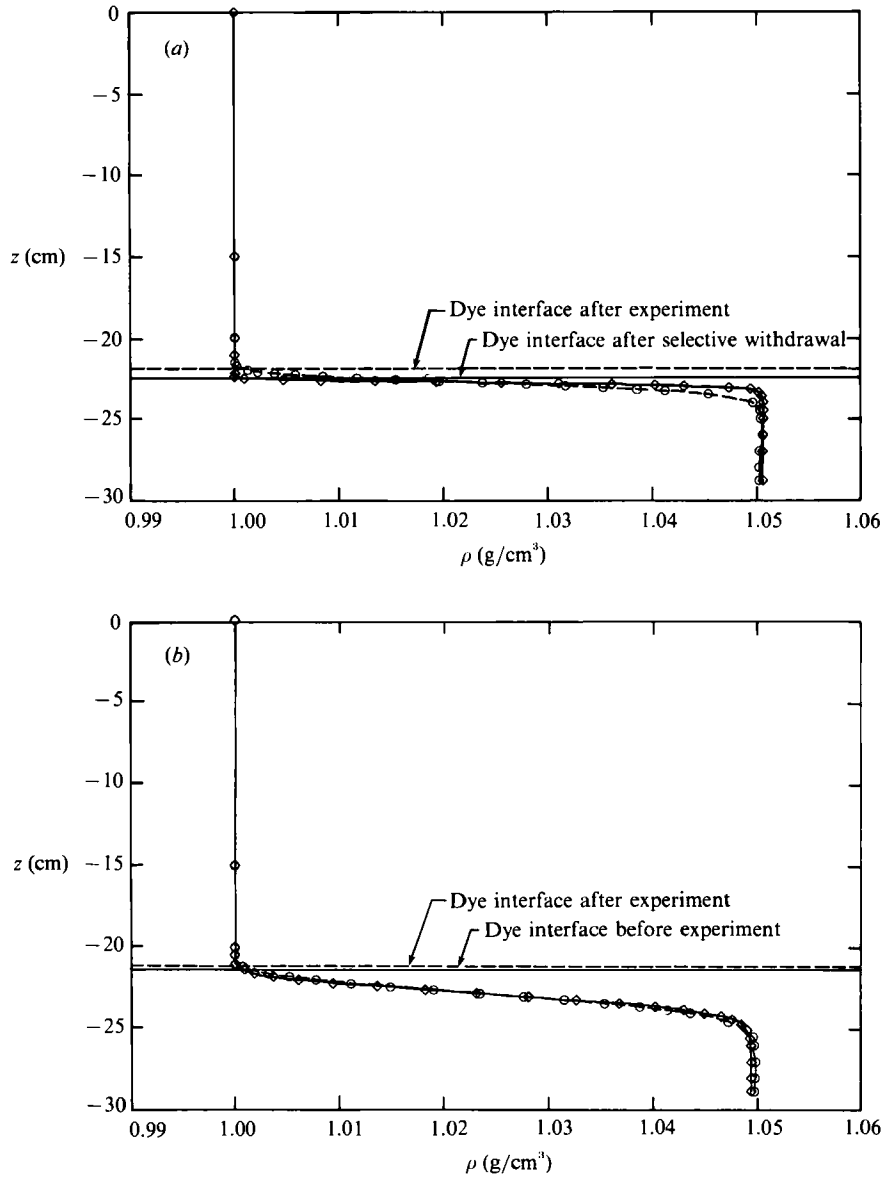

FIGURE 4. Experimental density profiles for $h_1 = 22.8$ cm and $h_2 = 7.6$ cm. (*a*) Sharp interface: —◇—, after selective withdrawal; —○—, after experiment. (*b*) Diffuse interface: —◇—, before experiment; —○—, after experiments.

116 min. Using (74), the apparent diffusion coefficient is found to be 1.94×10^{-5} cm^2 s^{-1}. Similarly, in figure 4(*b*) the interface thickness before and after experiment was 2.22 and 2.61 cm, respectively, and the time interval between measurements of the density profile was 115 min, which yield a value of the apparent diffusion coefficient of 2.17×10^{-5} cm^2 s^{-1}. The larger values of the apparent diffusion coefficient are attributed to wave-induced mixing. It should be noted that the internal waves in the trench were 'at resonance' in these two cases; the values of the apparent diffusion coefficient in most experiments were smaller than the above values.

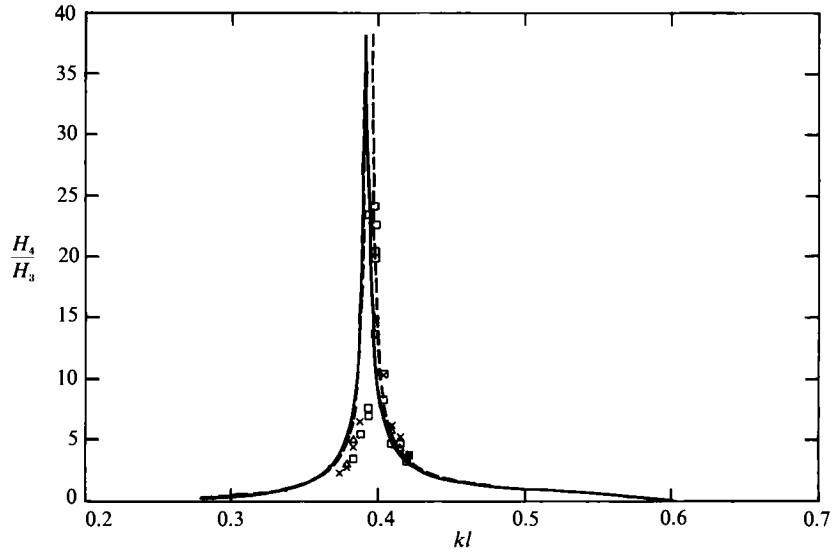

FIGURE 5. Response curves for internal waves for a sharp density interface. The theoretical results are computed using $h_1 = 22.15$ cm, $h_2 = 6.95$ cm, $\delta = 1.3$ cm, and $\rho_2/\rho_1 = 1.05$. □, $0.0035 < H_3/h < 0.01$; ×, $0.012 < H_3/h < 0.016$; △, $0.019 < H_3/h < 0.025$; —, three-layer viscous theory; ---, three-layer inviscid theory.

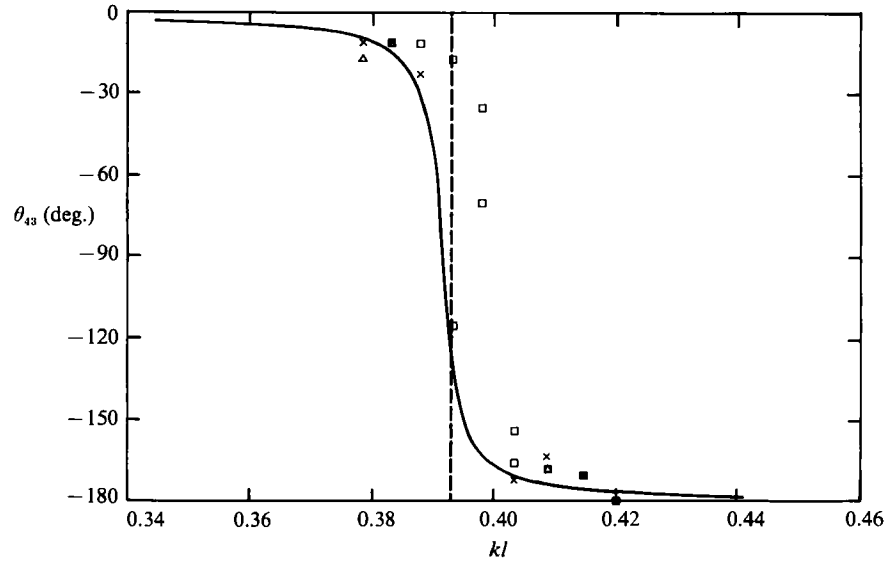

FIGURE 6. Relative phase angle between internal waves and surface waves. The theoretical results have the same conditions as in figure 5, and the symbols are the same as in figure 5.

In figure 5, the amplification factor of the internal wave, H_4/H_3, is plotted as a function of kl, where k is the wavenumber of the surface wave in the constant-depth channel and l is the trench width. The mean value of δ in these experiments was 1.32 cm, and the standard deviation was 0.12 cm. The mean density of salt water was 1.0497 g cm^{-3}, and the standard deviation was 0.00084 g cm^{-3}. The theoretical response curves are obtained using the three-layer model, with $\delta = 1.3$ cm, $\rho_2/\rho_1 = 1.05$, and $\nu = 1.0 \times 10^{-6}$ m^2 s^{-1}. The internal wave height at the top of the density

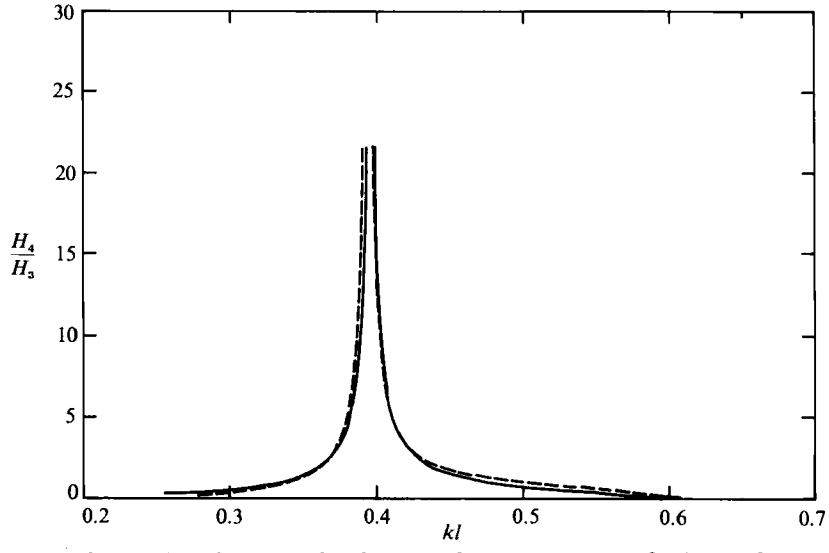

FIGURE 7. Comparison between the theoretical response curves for internal waves obtained using the two-layer model (—) and the three-layer model (----).

transition region is computed because the interfacial wave gauge measured motion of the dye interface, which can be seen in figure 4(*a*, *b*) to coincide with the top of the diffuse salinity interface. As shown in figure 5, the measured response curve is extremely peaked; the amplification factor H_4/H_3 attains a magnitude of about 24 at resonance. To either side of the resonant peak the response decreases rapidly. The inviscid solutions tend to infinity at resonance ($kl = 0.393$, $T = 7.80$ s). With damping, the maximum value of H_4/H_3 is 37.17 ($kl = 0.392$, $T = 7.83$ s). Comparing experiment to theory, energy dissipation in the actual fluid is seen to be larger than that predicted by the viscous theory, which assumes laminar flow in the boundary layers. Nevertheless, the agreement between experiment and theory is good, indicating that linear theory may be adequate for these experimental conditions. In figure 6, the relative phase angle between internal wave motion and surface wave motion, θ_{43}, is plotted as a function of the relative wavenumber, kl. The relative phase angle is defined between $-180°$ and $180°$. The results of theory and experiment both show a shift from in phase to out of phase through resonance.

In figure 7 the response curves obtained using a two-layer model (Ting & Raichlen 1988) and the three-layer model are compared for the inviscid case. From the two-layer model, the relative wavenumber kl corresponding to the lowest mode of resonance of internal waves is found to be 0.396 ($T = 7.75$ s). The effects of the density transition layer on the response curve are very small for these flow conditions; the difference between the wave periods of resonance obtained using the two wave models when compared to the difference between the wave periods of resonance of the first and second modes is less than 2%. This result is consistent with (21), which shows that for the surface mode and the primary internal mode the dispersion relation of a continuously stratified fluid of small density variations is similar to that of a two-layer fluid, if the thickness of the density interface is small compared to the wavelength of internal waves and the fluid depths. In these experiments, the values of $K_2\delta$, δ/h_1, and δ/h_2 were 0.07, 0.03 and 0.1, respectively, which are indeed much less than unity. We shall see that the effects of the diffuse interface on the response curve increase as δ increases and h_2 decreases.

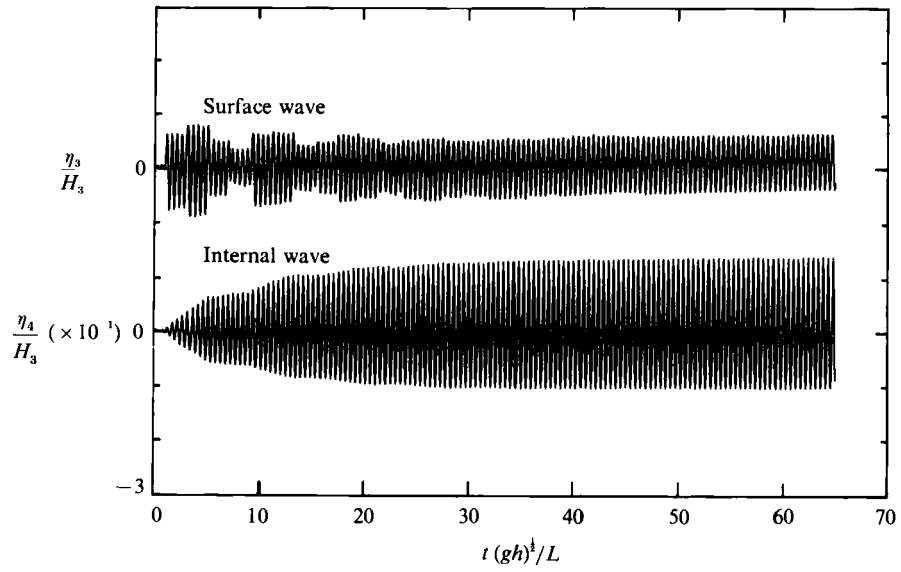

FIGURE 8. Experimental surface and internal wave time histories for $T = 7.7$ s ($kl = 0.398$) and $H_3 = 1.08$ mm.

The time histories of the internal waves and of the surface waves, from the start of the wave generator, are presented in figure 8 for a resonant condition of the internal waves in the trench. A characteristic beat pattern is seen in the surface wave record; this is due to transient wave motion in the wave tank. A beat pattern is absent from the internal wave record because this wave period corresponds to a resonant condition for the internal waves. However, the growth of the internal waves is retarded owing to the changing amplitude of the surface wave envelope above the trench.

An important feature shown in figure 8 is the symmetry of the internal wave profile about the mean, which suggests a linear model of wave–trench interaction for these experimental conditions. This is also supported by the good agreement between experiment and linear theory in the response curve shown in figure 5. To establish a range of validity for the linear theory, we shall study the internal waves in the trench.

Nonlinear standing internal waves have been studied by Thorpe (1968). For a two-layer fluid that completely fills a rectangular tank, the equation of the interface to second order for a small density difference is

$$\eta(x,t) = a\sin\sigma t\cos Kx + \frac{a^2K}{8T_1^2T_2^2}(T_1-T_2)(T_1T_2-3\cos 2\sigma t)\cos 2Kx, \tag{75}$$

where h_1, h_2 are the depths of the upper and the lower fluid, respectively, a is the wave amplitude, K is the wavenumber, and $T_i = \tanh Kh_i$ ($i = 1, 2$). Equation (75) does not depend on the wave generation mechanism, and is therefore suitable for investigating the general characteristics of standing internal waves. Thorpe (1968) also presented a more complicated result for a free upper surface. This is not used here because in the trench problem the internal wave mode is excited, the surface wave disturbance may be considered small and the solution for the interface tends to the solution for a fixed upper boundary.

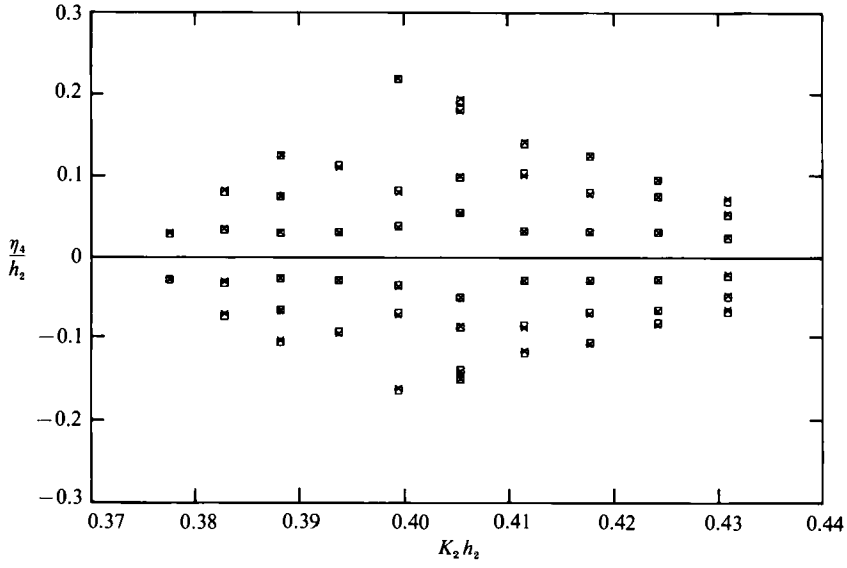

FIGURE 9. Comparison between the internal wave extrema for experiments (□) and second-order theory (equation (75)) (×).

The second-order term in (75) distorts the symmetric waveform of the linear solution given by the first-order term; the distance from trough to crest remains constant for the second-order approximation. Equation (75) is valid if the ratio of the coefficient of the second-order term to that of the first is much less than unity, that is, if

$$\left|\frac{aK(T_1-T_2)(3+T_1T_2)}{8T_1^2T_2^2}\right| \ll 1. \tag{76}$$

If one of the fluids is deep and the other shallow, of depth h, (76) reduces to

$$\frac{3H}{16Kh^2} \ll 1, \tag{77}$$

where $H = 2a$.

The contributions of second-order effects to the internal wave profile can be determined from (76) or (77) once the wave height is known. Conversely, (76) or (77) may be used to impose a limit on the linear theory. In figure 9, the wave extrema of internal waves, η_4, normalized by h_2, are plotted as a function of K_2h_2. These are shown for the same experiments that were presented in figure 5. The measured crest and trough amplitudes of internal waves are compared to the theoretical solutions of (75). In the theoretical solutions, the wavenumber K is computed using (19) for the internal wave mode, and the first-order wave amplitude a is assumed equal to the measured value of $\frac{1}{2}H_4$. Good agreement is seen between the observed and the computed wave amplitudes. This means that second-order effects in the internal wave motions are small, because (75) is only valid for weakly nonlinear waves. In figure 9, the maximum value of H_4/h_2 is 0.382 ($K_2h_2 = 0.399$). The corresponding ratio of the amplitude of the second-order term in (75) to that of the first is found to be 0.144, which indeed is much less than unity. In figure 10, the profiles of the density interface for a wave period of 7.7 s ($kl = 0.398$) are shown; the internal waves were near resonance. The agreement between the observed and the calculated wave

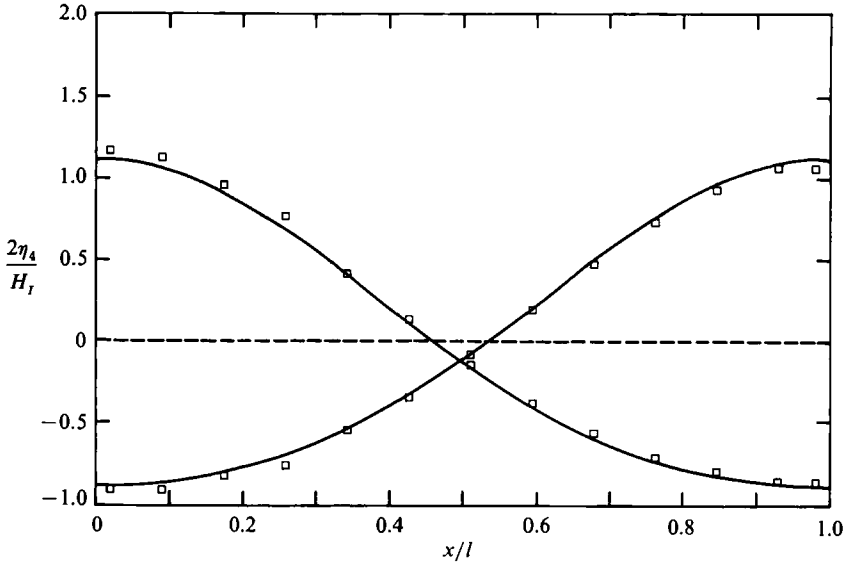

FIGURE 10. Internal wave profiles for the lowest mode of oscillation in the trench for $T = 7.7$ s and $H_4 = 2.4$ cm: □, experiments; —, second-order inviscid theory.

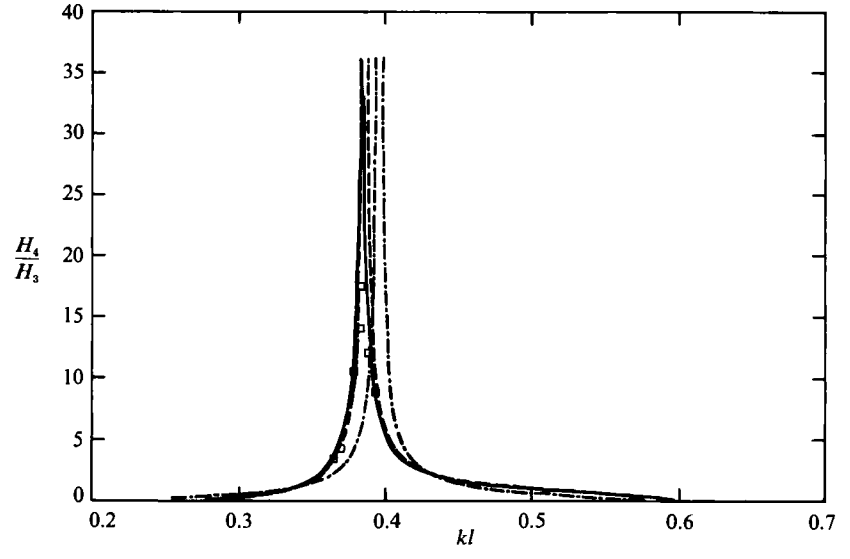

FIGURE 11. Response curves for internal waves for a diffuse density interface. The response curves by the three-layer model are for $h_1 = 21.55$ cm, $h_2 = 6.35$ cm, $\delta = 2.5$ cm, and $\rho_2/\rho_1 = 1.05$. □, Experiment; —, three-layer viscous theory; – – –, three-layer inviscid theory; –·–·–, two-layer inviscid theory.

profiles is quite good. Note that the standing internal waves do not have a true node at $x/l = 0.5$ owing to second-order effects in the wave profiles. Figures 9 and 10 show that the good agreement between experiment and linear theory observed in the response curves in figure 5 is indeed associated with weakly nonlinear internal waves in the trench.

The experimental results for an interface thickness of 2.5 cm are shown in figure 11. For these experiments, the mean value of δ was 2.46 cm, and the standard deviation

was 0.06 cm; the mean density of salt water was 1.0507 g cm^{-3}, and the standard deviation was 0.0005 g cm^{-3}. There is a small but definite shift in the resonant frequency of the internal waves compared to that predicted by the two-layer model; the difference between the wave periods of resonance for the lowest mode obtained using the two-layer model and the three-layer model when compared to the difference between the wave periods of the first and the second resonant modes is about 6%. The relative wavenumber kl corresponding to the lowest mode of resonance as predicted by the two-layer inviscid model, the three-layer inviscid model, and the three-layer viscous model, respectively, are 0.396, 0.386, and 0.383. The corresponding wave periods are 7.75, 7.95, and 7.99 s. The effect of increasing the thickness of the density interface is to decrease the resonance frequency. This is because the density of the quiescent fluid, $\bar{\rho}$, which represents the inertia of the fluid, is almost unchanged by increasing the interface thickness, whereas the restoring force responsible for the existence of wave motion, represented by $g\eta\,\mathrm{d}\bar{\rho}/\mathrm{d}z$, where η is the vertical displacement of a fluid element from its undisturbed position, decreases as δ increases. The frequency of the motion will decrease with smaller restoring force, which is the case shown here. Comparing figure 11 to figure 5 it is seen that the magnitude of the amplification factor obtained using the three-layer model, is relatively insensitive to these changes in the thickness of the density interface.

4.2. *Experiments with a shallow lower fluid in the trench*

For finite-amplitude standing waves at the interface of two fluids of small density difference, the ratio of the coefficient of the second-order term in the wave profile to that of the first is given by (76). This ratio reduces to $3H/16Kh^2$ when one of the fluids is deep and the other shallow of depth h. The linear theory predicted the wave motion in the trench quite well when the value of this parameter was much less than unity. Because the dimensionless parameter H/Kh^2 varies inversely as the square of the depth h, it is expected that nonlinear effects in internal waves in the trench will be more important as the depth of the lower fluid h_2 decreases. However, the rate of viscous dissipation in the bottom boundary layer, normalized by the energy density of internal waves, is proportional to $\sigma^2(\frac{1}{2}\nu\sigma)^{\frac{1}{2}}/(g\Delta\rho/\rho_1)/\sinh^2 K_2 h_2$. The effect of decreasing h_2 is to increase the horizontal velocity next to the trench bottom and to decrease the resonant frequency. The net result is to increase the shearing motions in the bottom boundary layer and hence the viscous dissipation rate. In a shallow lower fluid, the effects of nonlinearity and dissipation may compete with each order and thus produce more complicated behaviour. To investigate this, the depth of the lower fluid h_2 was reduced to 3.8 cm, while the total depth of the fluid in the trench and the density difference between layers were kept fixed. Thus, the value of $H_4/K_2 h_2^2$ would be increased fourfold for the same wave height H_4 and wavenumber K_2 of the internal wave.

In figure 12, the amplification factor H_4/H_3 is plotted as a function of kl for the lowest resonant mode. For these experiments, the mean value of δ was 1.31 cm and the standard deviation was 0.09 cm; the mean value of ρ_2 was 1.0506 g cm^{-3}, and the standard deviation was 0.0008 g cm^{-3}. The theoretical response curves are computed using $\delta = 1.3$ cm and $z = -25.95$ cm. The three-layer inviscid model predicts that resonance of the internal wave will occur at $kl = 0.306$ ($T = 10.05$ s). In comparison, the two-layer inviscid model predicts that resonance will occur at $kl = 0.31$ ($T =$ 9.9 s). The difference between the wave periods of resonance predicted by the two wave models, when compared to the difference between the wave periods of the first and second modes of resonance, is 3.3%. This compares to a value of less than 2%

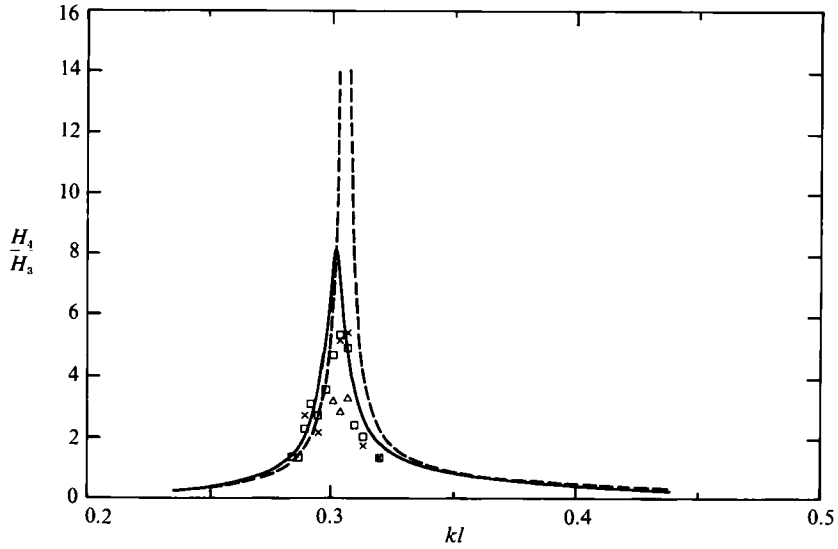

FIGURE 12. Response curves for internal waves for a sharp density interface. The theoretical results are computed using $h_1 = 25.95$ cm, $h_2 = 3.15$ cm, $\delta = 1.3$ cm, and $\rho_2/\rho_1 = 1.05$. □, $0.013 < H_3/h < 0.023$; ×, $0.027 < H_3/h < 0.045$; △, $0.076 < H_3/h < 0.082$; —, three-layer viscous theory; ---, three-layer inviscid theory.

for the case of the deep lower fluid, reflecting this increase in the effect of the density transition layer on the internal wave motions in the trench. This is not a surprising result because from (21) we expect that the density transition region should have a more pronounced effect on the response curve for a larger value of δ/h_2. Nevertheless, the wave period of resonance predicted by the two-layer model is sufficiently accurate for these experimental conditions; we should expect greater errors as the value of δ/h_2 increases.

Comparing figure 12 to figure 5, the amplitudes of internal waves have decreased substantially through the decrease in h_2. As the relative depth $K_2 h_2$ is reduced from 0.4 to 0.2, the theoretical prediction of the amplification factor H_4/H_3 at resonance decreases from 37.17 to 8.2, and the observed value of H_4/H_3 decreases from 24 to 6 approximately. There is a less notable difference in the frequencies of resonance predicted by the inviscid theory and the viscous theory. With damping, the three-layer model predicts that the resonant peak occurs at $kl = 0.301$ ($T = 10.17$ s). This compares to a value of kl of 0.306 ($T = 10.05$ s) from the three-layer inviscid model. Increases in viscous effects can also be seen from the variation of relative phase angle between internal wave motion and surface wave motion (figure 13). In comparison with figure 6, both theory and experiment show a more gradual change of θ_{43} from in phase to out of phase through resonance, reflecting this increase in viscous dissipation. It is noted that in these experiments, viscous dissipation in the trench was concentrated in two regions: in the boundary layer adjacent to the trench bottom, and in the boundary layers next to the sidewalls. In comparison, the energy loss at the trench walls at $x = 0$ and $x = l$ was very small. This is because the horizontal component of the fluid velocity was much larger than the vertical component for the lowest mode of oscillation. In addition, the total energy loss in the upper fluid was much smaller than that in the lower fluid because, for the internal waves, the water particle velocities decreases rapidly with distance from the density interface in the upper fluid but they decrease much more slowly in the lower fluid.

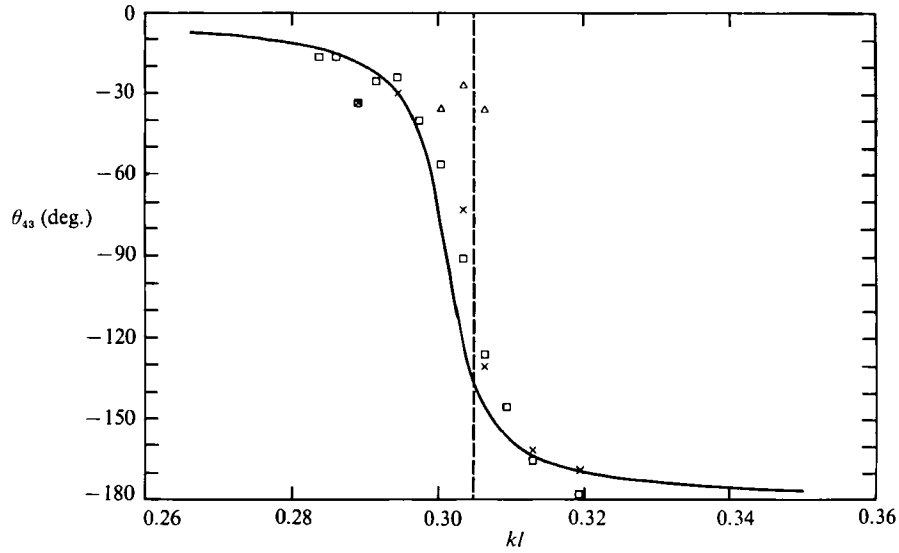

FIGURE 13. Relative phase angle between internal waves and surface waves. The theoretical results have the same conditions as in figure 12, and the symbols are the same as in figure 12.

In fact, owing to the long waves used, the amplitude of the horizontal velocity was almost uniform with depth in the lower fluid. This means that the energy loss attributed to the trench bottom and to the sidewalls should be roughly in proportion to the surface areas b/h_2, which is 5.2. Hence, the bottom boundary layer was the prime source of viscous dissipation in these experiments.

Figure 12 indicates that viscous dissipation in the actual fluid was somewhat larger than that predicted by laminar flow. Nevertheless, the agreement between experiment and linear theory is good, even though nonlinear effects are significant in this problem. Nonlinear effects were clearly seen in the wave profiles of internal waves. In figure 14 the time histories of the internal waves and of the surface waves are presented for a wave period of 10 s, which corresponds to a resonant condition in the trench. As seen in figure 14 the waveforms of the internal waves are non-symmetrical about the quiescent density (dye) interface, whereas the waveforms of the surface waves appear to be symmetrical about the mean water level. The latter indicates that nonlinear effects in the surface wave profiles are small. It is also important to note that the response curve of figure 12 results in an efficient filter for frequencies away from resonance, so that the high-frequency components in the surface waves contribute very little to the motion of the internal waves. Thus, the non-symmetrical waveforms observed in the internal wave record are due to truly nonlinear behaviour in the internal wave motions.

The linear theory is reasonably good in predicting the resonant frequency and the shape of the response curve, but it describes the wave profile poorly. The ratio of the crest amplitude to the trough amplitude of the internal wave in figure 14 is 3.1 at steady state. It is interesting to compute the ratio of the second-order term in (75) to that of the first, even though the solution given by (75) is clearly invalid for these experimental conditions. From (75), with $H_4/h_2 = 1.079$, $K_2 h_1 = 1.393$, and $K_2 h_2 = 0.199$, we obtain an amplitude ratio of 0.972 for the second-order term, which is indeed large, indicating that nonlinear effects are important. We also note that the wave heights of internal waves were large compared to the depth of the lower fluid.

The time evolution of the density interface across the trench is presented in figure

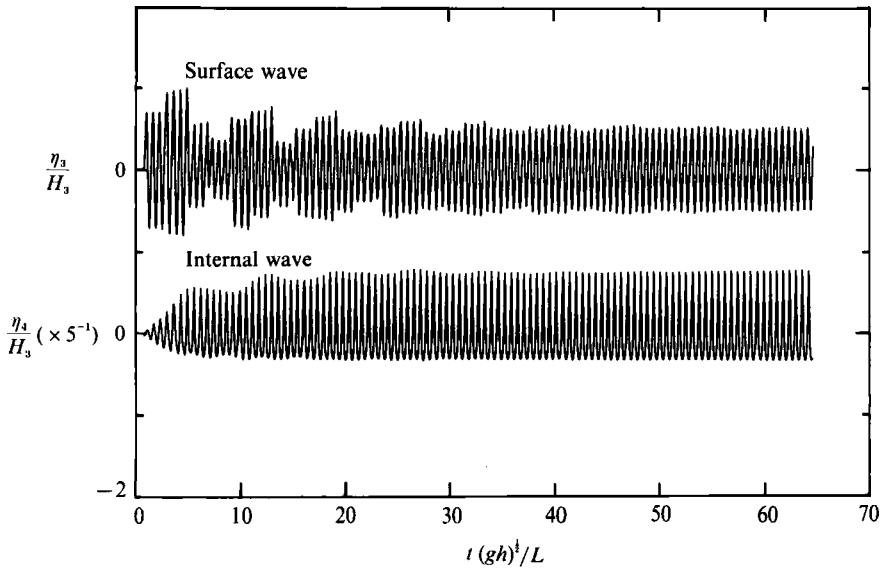

FIGURE 14. Experimental surface and internal wave time histories for $T = 10.0$ s ($kl = 0.306$) and $H_3 = 4.95$ mm.

15. The data points were obtained from the steady-state wave records; the elevations of the density interface at different locations across the trench were obtained by matching the phase of the surface waves. The travelling wave pattern is clearly seen; the internal wave looks like a single 'hump' of fluid travelling back and forth in the trench. It is evident that Thorpe's finite-amplitude wave theory cannot describe these internal waves. The results of a study by Helal & Molines (1981) indicate that this class of nonlinear internal waves can be modelled by shallow water wave theory. Helal & Molines (1981) conducted experiments in a rectangular tank that was partially filled with a two-layer fluid of fresh water and salt water; the fluid depths were small compared to the length of the tank. Helal & Molines generated internal waves by oscillating the tank horizontally in a sinusoidal manner at the resonant frequencies of the internal waves. They also constructed a theoretical solution for the internal waves in the tank in the form of two internal cnoidal waves of the same amplitude travelling in opposite directions. Helal & Molines showed experimentally that the waves in the oscillating tank could be represented by a linear superposition of cnoidal-shaped waves and a sine wave shape; the sine wave component was due to the oscillatory motion of the tank. For navigation trenches, travelling internal waves like those shown in figure 15 are perhaps of greater practical importance than the standing internal waves shown in figure 10, because the width of navigation channels, and the wavelength of internal waves, are typically much larger than the fluid depths. A formulation based on shallow-water wave theory including viscous dissipation would be useful for investigating this problem.

Finally, we present in figure 16 the results of those experiments where the interface thickness was 2.5 cm. In these experiments, the mean value of δ was 2.44 cm, and the standard deviation was 0.04 cm; the mean density of the lower fluid (salt water) was 1.0496 g cm^{-3}, and the standard deviation was 0.0017 g cm^{-3}. Also shown in figure 16 are the theoretical solutions of the three-layer model and the two-layer model. The solutions of the three-layer model are computed using $z = -25.35$ cm and $\delta = 2.5$ cm. The relative wavenumber kl at resonance as predicted by the two-layer

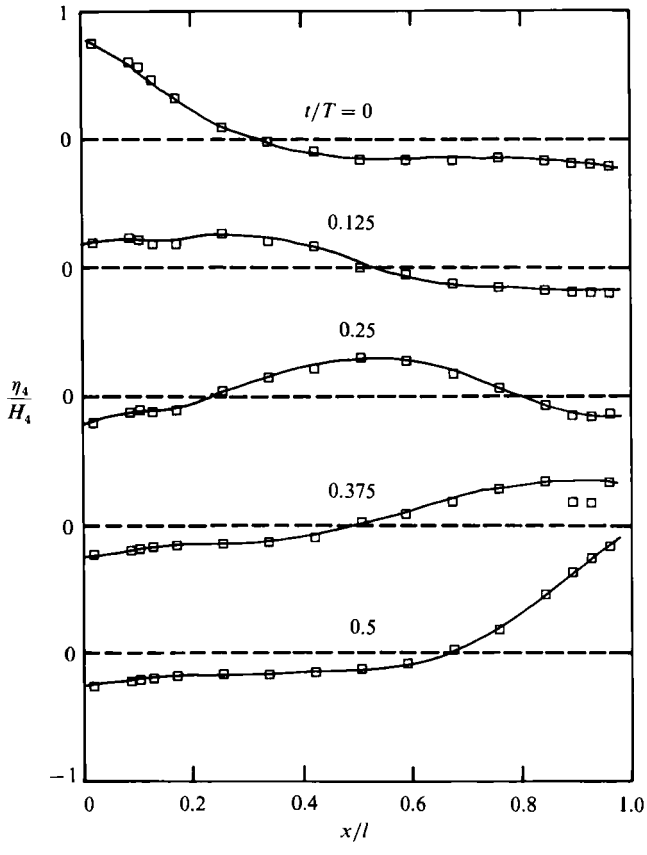

FIGURE 15. Time evolution of the density interface in the trench for $T = 10.0$ s and $H_4/h_2 = 1.079$.

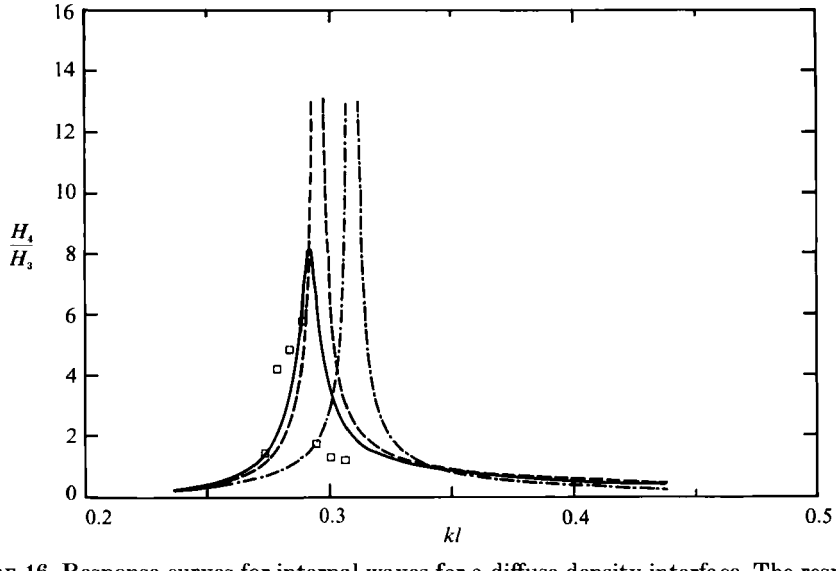

FIGURE 16. Response curves for internal waves for a diffuse density interface. The response curves by the three-layer model are for $h_1 = 25.35$ cm, $h_2 = 2.55$ cm, $\delta = 2.5$ cm, and $\rho_2/\rho_1 = 1.05$. □, Experiments; —, three-layer viscous theory; ---, three-layer inviscid theory; ·--, two-layer inviscid theory.

inviscid model, the three-layer inviscid model, and the three-layer viscous model are 0.31, 0.295 and 0.292, respectively. The corresponding wave periods are 9.9, 10.38, and 10.51 s. The difference between the wave periods of resonance predicted by the two-layer inviscid model and the three-layer inviscid model when compared to the difference between the wave periods of the first and the second modes of resonance is about 11%. The limited experimental data available tend to support the predictions of the three-layer model. Figure 16 emphasizes the importance of including the density transition region to correctly predict the response curve for internal waves in a shallow lower fluid.

5. Conclusions

To examine the interaction of water waves with a density-stratified fluid in a rectangular trench, a linear model was developed for steady-state flow conditions, and experiments were conducted in which internal wave motions at the interface of a stratified fluid of fresh water and salt water were measured using a laser-optics detector system. In the theoretical model, the density distribution in the trench was approximated by two homogeneous fluids of different densities separated by a transition region of linear density variation, and viscous effects were treated based on the assumption of a laminar boundary layer. Internal wave profiles obtained by experiments were compared to Thorpe's finite-amplitude wave theory. The following main conclusions can be drawn from this investigation:

(i) The three-layer model predicts the response curve based on internal wave height quite well in all the cases investigated, even when nonlinear effects are important. The effects of viscosity and of a diffuse density interface on the response curve are also predicted well by the three-layer model.

(ii) When the ratio of internal wave height to the depth of lower fluid, H/h_2, is small compared to the dimensionless wavenumber for the internal wave $K_2 h_2$, the profiles of internal waves in the trench at steady state obtained by experiment compare well to the standing wave shape of Thorpe's finite-amplitude wave theory.

(iii) Nonlinear effects in internal wave motions were more apparent when the value of $H/K_2 h_2^2$ was increased by decreasing the depth of the lower fluid h_2. The observed waveforms were non-symmetrical about the quiescent density interface, and the internal wave motions looked like a single 'hump' of fluid travelling back and forth inside the trench.

(iv) The frequency of resonance of the trench decreases as the thickness of the density interface increases; the frequency shift is predicted well by the three-layer model. When the thickness of the density interface is large compared to the depth of the lower fluid, the response curves for internal waves obtained using the two-layer model and three-layer model differ significantly.

(v) The response curve for internal waves is very sensitive to viscous effects. When the depth of the lower fluid is small compared to the wavelength of internal waves, viscous dissipation in the trench bottom boundary layer greatly reduces the amplitudes of internal waves and hence the effects of trench resonance.

This work was funded by the Office of Naval Research under contract N00014-84-C-0617 and was conducted when the author was a graduate student at the California Institute of Technology. The guidance of Professor Fredric Raichlen, and the support of the faculty and staff of the W. M. Keck Laboratory of Hydraulics and Water Resources are deeply appreciated.

Appendix

The following quantities are used in the text:

$$Z(z) = (\Lambda^h)^{-\frac{1}{2}} \sinh k(z+h), \tag{A 1}$$

$$\hat{Z}_n(z) = (\Lambda_n^h)^{-\frac{1}{2}} \sin \hat{k}_n(z+h) \quad (n = 1, 2, \ldots), \tag{A 2}$$

$$\Lambda^h = -\frac{1}{2}\left(\frac{1}{2k}\sinh 2kh - h\right) + \frac{g}{\sigma^2}\sinh^2 kh, \tag{A 3}$$

$$\Lambda_n^h = \frac{1}{2}\left(\frac{1}{2\hat{k}_n}\sin 2\hat{k}_n h - h\right) + \frac{g}{\sigma^2}\sin^2 \hat{k}_n h, \tag{A 4}$$

$$Z_{j1}(z) = (\Lambda_j^s)^{-\frac{1}{2}}(\Theta^{\frac{1}{2}}\cos(\Theta^{\frac{1}{2}}K_j\delta) + \coth K_j h_2 \sin(\Theta^{\frac{1}{2}}K_j\delta)) \times \frac{K_0\cosh K_j z + K_j \sinh K_j z}{K_0\cosh K_j h_1 - K_j \sinh K_j h_1} \quad (j = 1, 2, \ldots), \tag{A 5}$$

$$Z_{j2}(z) = (\Lambda_j^s)^{-\frac{1}{2}}\Theta^{\frac{1}{2}}\frac{\sinh K_j(z+h_1+h_2+\delta)}{\sinh K_j h_2}, \tag{A 6}$$

$$Z_{j3}(z) = (\Lambda_j^s)^{-\frac{1}{2}}(\Theta^{\frac{1}{2}}\cos(\Theta^{\frac{1}{2}}K_j(z+h_1+\delta)) + \coth K_j h_2 \sin(\Theta^{\frac{1}{2}}K_j(z+h_1+\delta))), \tag{A 7}$$

$$\hat{Z}_{n1}(z) = (\Lambda_n^s)^{-\frac{1}{2}}(\Theta^{\frac{1}{2}}\cosh(\Theta^{\frac{1}{2}}\hat{K}_n\delta) + \cot \hat{K}_n h_2 \sinh(\Theta^{\frac{1}{2}}\hat{K}_n\delta)) \times \frac{K_0\cos \hat{K}_n z - \hat{K}_n \sin \hat{K}_n z}{K_0\cos \hat{K}_n h_1 + \hat{K}_n \sin \hat{K}_n h_1} \quad (n = 1, 2, \ldots), \tag{A 8}$$

$$\hat{Z}_{n2}(z) = (\Lambda_n^s)^{-\frac{1}{2}}\Theta^{\frac{1}{2}}\frac{\sin \hat{K}_n(z+h_1+h_2+\delta)}{\sin \hat{K}_n h_2}, \tag{A 9}$$

$$\hat{Z}_{n3}(z) = (\Lambda_n^s)^{-\frac{1}{2}}(\Theta^{\frac{1}{2}}\cosh(\Theta^{\frac{1}{2}}\hat{K}_n(z+h_1+\delta)) + \cot \hat{K}_n h_2 \sinh(\Theta^{\frac{1}{2}}\hat{K}_n(z+h_1+\delta))), \tag{A 10}$$

$$\Lambda_j^s = -\frac{h_2\Theta}{2\sinh^2 K_j h_2}\left(\frac{\sinh 2K_j h_2}{2K_j h_2} - 1\right) + \tfrac{1}{2}\Theta\delta\left\{\left(\frac{\sin(2\Theta^{\frac{1}{2}}K_j\delta)}{2\Theta^{\frac{1}{2}}K_j\delta} + 1\right)\Theta - \frac{\coth K_j h_2}{K_j\delta}(\cos(2\Theta^{\frac{1}{2}}K_j\delta) - 1) - \coth^2 K_j h_2\left(\frac{\sin(2\Theta^{\frac{1}{2}}K_j\delta)}{2\Theta^{\frac{1}{2}}K_j\delta} - 1\right)\right\} - \frac{1}{2}\left\{K_0^2 h_1\left(\frac{\sinh 2K_j h_1}{2K_j h_1} + 1\right) - K_0(1+\cosh 2K_j h_1) + K_j^2 h_1\left(\frac{\sinh 2K_j h_1}{2K_j h_1} - 1\right)\right\} \times \left(\frac{\Theta^{\frac{1}{2}}\cos(\Theta^{\frac{1}{2}}K_j\delta) + \coth K_j h_2 \sin(\Theta^{\frac{1}{2}}K_j\delta)}{K_0\cosh K_j h_1 - K_j \sinh K_j h_1}\right)^2, \tag{A 11}$$

$$\Lambda_n^s = \frac{h_2\Theta}{2\sin^2 \hat{K}_n h_2}\left(\frac{\sin 2\hat{K}_n h_2}{2\hat{K}_n h_2} - 1\right) + \tfrac{1}{2}\Theta\delta\left\{\left(\frac{\sinh(2\Theta^{\frac{1}{2}}\hat{K}_n\delta)}{2\Theta^{\frac{1}{2}}K_n\delta} + 1\right)\Theta + \frac{\cot \hat{K}_n h_2}{\hat{K}_n\delta}(\cosh(2\Theta^{\frac{1}{2}}\hat{K}_n\delta) - 1) + \cot^2 \hat{K}_n h_2\left(\frac{\sinh(2\Theta^{\frac{1}{2}}\hat{K}_n\delta)}{2\Theta^{\frac{1}{2}}K_n\delta} - 1\right)\right\} - \frac{1}{2}\left\{K_0^2 h_1\left(\frac{\sin 2\hat{K}_n h_1}{2\hat{K}_n h_1} + 1\right) - K_0(1+\cos 2\hat{K}_n h_1) - \hat{K}_n^2 h_1\left(\frac{\sin 2\hat{K}_n h_1}{2\hat{K}_n h_1} - 1\right)\right\} \times \left(\frac{\Theta^{\frac{1}{2}}\cosh(\Theta^{\frac{1}{2}}\hat{K}_n\delta) + \cot \hat{K}_n h_2 \sinh(\Theta^{\frac{1}{2}}\hat{K}_n\delta)}{K_0\cos \hat{K}_n h_1 + \hat{K}_n \sin \hat{K}_n h_1}\right)^2. \tag{A 12}$$

REFERENCES

BENJAMIN, T. B. 1966 Internal waves of finite amplitude and permanent forms. *J. Fluid Mech.* **25**, 241–270.

BENJAMIN, T. B. 1967 Internal waves of permanent form in fluids of great depth. *J. Fluid Mech.* **29**, 559–592.

DORE, B. D. 1969*a* A contribution to the theory of viscous damping of stratified wave flows. *Acta Mech.* **8**, 25–33.

DORE, B. D. 1969*b* The decay of oscillations of a non-homogeneous fluid within a container. *Proc. Camb. Phil. Soc.* **65**, 301–307.

HEAD, M. J. 1983 The use of miniature four-electrode conductivity probes for high resolution measurement of turbulent density or temperature variations in salt-stratified water flows. Ph.D. thesis, University of California, San Diego.

HELAL, M. A. & MOLINES, J. M. 1981 Non-linear internal waves in shallow water. A theoretical and experimental study. *Tellus* **33**, 488–504.

HUNT, J. N. 1961 Interfacial waves of finite amplitude. *La Houille Blanche* **16**, 515–525.

KIRBY, J. T. & DALRYMPLE, R. A. 1983 Propagation of obliquely incident water waves over a trench. *J. Fluid Mech.* **133**, 47–63.

LEE, J. J. & AYER, R. M. 1981 Wave propagation over a rectangular trench. *J. Fluid Mech.* **110**, 335–347.

MARINE BOARD (NATIONAL RESEARCH COUNCIL) 1983 *Criteria for the Depths of Dredged Navigational Channels.* Washington, DC: National Academy Press.

MEI, C. C. & LIU, L. F. 1973 The damping of surface gravity waves in a bounded liquid. *J. Fluid Mech.* **59**, 239–256.

MILES, J. W. 1982 On surface-wave diffraction by a trench. *J. Fluid Mech.* **115**, 315–325.

THORPE, S. A. 1968 On standing internal gravity waves of finite amplitude. *J. Fluid Mech.* **32**, 489–528.

TING, C. K. F. & RAICHLEN, F. 1986 Wave interaction with a rectangular trench. *J. Waterway, Port, Coastal Ocean Engng. Div., ASCE* **112**, 454–460

TING, C. K. F. & RAICHLEN, F. 1988 Wave interaction with rectangular trench in density-stratified fluid. *J. Waterway, Port, Coastal Ocean Engng. Div., ASCE* **114**, 615–636.

YIH, C. S. 1980 *Stratified Flows.* Academic.